Microfluidic extensional rheometry using stagnation point flow

S. J. Haward[a)]
Okinawa Institute of Science and Technology Graduate University, Onna, Okinawa 904-0495, Japan

(Received 22 December 2015; accepted 1 February 2016; published online 5 April 2016)

Characterization of the extensional rheometry of fluids with complex microstructures is of great relevance to the optimization of a wide range of industrial applications and for understanding various natural processes, biological functions, and diseases. However, quantitative measurement of the extensional properties of complex fluids has proven elusive to researchers, particularly in the case of low viscosity, weakly elastic fluids. For some time, microfluidic platforms have been recognized as having the potential to fill this gap and various approaches have been proposed. This review begins with a general discussion of extensional viscosity and the requirements of an extensional rheometer, before various types of extensional rheometers (particularly those of microfluidic design) are critically discussed. A specific focus is placed on microfluidic stagnation point extensional flows generated by cross-slot type devices, for which some important developments have been reported during the last 10 years. Additional emphasis is placed on measurements made on relevant biological fluids. Finally, the operating limits of the cross-slot extensional rheometer (chiefly imposed by the onset of elastic and inertial flow instabilities) are discussed. © *2016 AIP Publishing LLC*.
[http://dx.doi.org/10.1063/1.4945604]

I. INTRODUCTION

Extensional flows arise whenever there are streamwise velocity gradients present in a flow field. Classical examples of flows with strong extensional components include changes in flow cross-sectional area (i.e., contractions and expansions),[1] thinning fluid filaments (jetting, dripping, etc.),[2] and flows with stagnation points (flow around obstacles and through bifurcations, for example).[3] The extensional deformation of fluid elements plays a significant and often vital role in a vast number of natural and industrial processes and applications. Important and often-cited examples include fiber-spinning, film-blowing, ink-jet printing, turbulent drag reduction, and porous media flows (e.g., filtration and enhanced oil recovery, EOR).[4–9] Extensional components also exist in *in-vivo* flows of physiological fluids such as blood,[10,11] mucus,[12,13] and synovial fluid.[14,15] Most of these processes involve the flow of fluids with a complex microstructure composed of synthetic polymers, polysaccharides, or proteins, which are characterized by the ability to undergo significant deformation given sufficiently strong hydrodynamic forces. In general, microstructural deformation becomes significant if the streamwise velocity gradient (or strain rate, $\dot{\varepsilon}$) exceeds the rate at which the microstructure can relax ($1/\lambda$, where λ is the characteristic relaxation time of the fluid).[16,17] In fact, it is found that deformation occurs when the dimensionless Weissenberg number $\mathrm{Wi} = \lambda\dot{\varepsilon} \gtrsim 0.5$.[18,19] Trouton showed that Newtonian fluids in uniaxial purely extensional flows exhibit an extensional viscosity η_E exactly 3 times higher than the viscosity η expected in a purely shearing deformation, such that the Trouton ratio $\mathrm{Tr} = \eta_E/\eta = 3$.[20] However, complex fluids in extensional flows at above $\mathrm{Wi} = 0.5$ may show orders-of-magnitude increases in the extensional viscosity and hence $\mathrm{Tr} \gg 3$.[21–24] This extension-thickening is the vital property of complex fluids that is harnessed in controlling the

a)Electronic mail: simon.haward@oist.jp

stability or breakup of filaments in fiber-spinning and inkjet printing and in controlling viscous fingering and generating high pressures for purposes of EOR. In the natural world, the extensional viscosity contributes to the properties required from glues used on spider webs and by carnivorous plants,[25–27] protein solutions used by spiders and insects for the spinning of silk,[28] and that controls many of the functions of mucus.[12,13,29,30]

The extensional viscosity is recognized as a fundamental material function that needs to be quantified in order to enable a full predictive description of the response of a particular fluid to an arbitrary applied deformation through the development of an accurate constitutive equation.[31,32] However, the extensional viscosity has proved to be an extremely difficult and elusive quantity to measure.[22,33] While methods of applying steady homogeneous and viscometric shearing deformations to a fluid are well established and reliable (by using, for example, cone-plate or Taylor-Couette geometries in torsional rheometers), the same is not true for extensional flows.[34] An ideal purely extensional flow is described by a deformation rate tensor that only has non-zero elements on its diagonal and is thus shear and vorticity free.[33] In practice, it is extremely difficult (perhaps impossible) to apply a purely extensional deformation to a bulk sample of a mobile liquid; there are always surfaces and/or interfaces at which an element of shear will be present, in which case shearing contributions to the measured quantities (i.e., stress) should be corrected for. A second problem with measuring the extensional viscosity is its dependence on both the applied strain rate $\dot{\varepsilon}$ and the accumulated fluid strain $\varepsilon(t) = \dot{\varepsilon}t$, where t is the time. This problem is complicated because the transfer of strain from a deformed fluid element to the dissolved or suspended fluid microstructure contained within is generally non-affine, and the degree of affinity also depends on the rate of strain, or equivalently on the Wi.[19,35] Most techniques report what is commonly referred to as a "transient" extensional viscosity since the strain rate is applied for a limited time period so that limited microstructural strain can be accumulated in the system. In order to observe a steady-state extensional viscosity, a persistent extensional flow is required; in other words, the applied strain rate $\dot{\varepsilon}$ must be maintained for long enough times that the microstructural strain can reach saturation at that rate. This requirement is most readily achieved at a stagnation point, where the residence time is arbitrarily long. A third problem regarding extensional rheometry with complex fluids is the occurrence of viscoelastic flow instabilities. Instabilities affect all kinds of rheometric techniques, but this particularly applies to extensional flows because the deformations and elastic stresses involved are generally much greater than they are in shearing flows. A fourth problem is establishing a consistent and reliable initial condition.[32,34] In many techniques (e.g., flow through contraction geometries), the fluid has to flow into the measurement region where the extensional flow field is applied (i.e. the contraction throat), so the prior flow deformation history of fluid elements also comes into question. Considering these factors, it is not too surprising that extensional viscosity measurements of a single model fluid by different techniques can yield results spread over several orders of magnitude.[22] Trying to measure the extensional viscosity can sometimes seem like a hopeless task, but the problem is important and interesting enough to motivate continued efforts. Even if a true measure of the $\eta_E(\dot{\varepsilon}, \varepsilon)$ cannot be obtained, tests with an extensional rheometer with a configuration that appropriately models the particular application of interest are worthwhile as they can give valuable information about the rheological response of a particular complex fluid.

There now exist a variety of options for performing extensional testing on mobile fluid samples, all of which come with their own advantages and disadvantages and which tend to be appropriate for particular kinds of fluids. Microfluidic technologies have been recognized as having the potential to probe the extensional rheological response of the most challenging kinds of fluid samples, those with low viscosity η and low elasticity (or short relaxation times). This is because the inherently small length scales of microfluidic devices mean that high deformation rates (i.e., high Wi) can be achieved while minimizing inertia (i.e., for low Reynolds number, $\mathrm{Re} = \rho U l/\eta$, where ρ is the fluid density, U is the flow velocity, and l is the characteristic length scale).[36] Also due to the small length scales, microfluidic devices offer a platform for the study of fluids for which only small sample quantities are available, as is the case for many biological samples. The ability to test and characterize the properties of small volumes of

biological specimens in microfluidic devices offers new opportunities in the fields of medical diagnostics and therapeutics, and for enhancing the fundamental understanding of the functional mechanisms of the fluids.[37–40]

The remainder of this review is organized as follows: in Section II, we will critically discuss some of the existing methods for applying extensional deformations to mobile fluids in order to contextualize the contribution of microfluidics to the field. These methods are broadly subdivided into the categories of "filament thinning," "contraction flows," and "stagnation point flows." In Section III, we will focus attention on the specific example of stagnation point flow within the microfluidic cross-slot geometry, briefly discussing the wider application of the device in microfluidic research applications before concentrating on its specific use as an extensional rheometer in Section IV. We will highlight recent progress in physical understanding and in technological advances that have resulted in a few significant recent developments. We will also place some emphasis on investigations involving biological fluid samples that can be particularly challenging to measure due to their complex composition and properties. In Section IV C, we will discuss the limitations of the technique arising from the onset of elastic and inertial flow instabilities, before discussing the general outlook for the cross-slots and the potential for future developments of this microfluidic extensional rheometry technique in Section V.

II. METHODS OF GENERATING EXTENSIONAL FLOW FIELDS

A. Thinning of fluid filaments

Probably the closest approximations to homogeneous extensional flows are produced by Filament Stretching Extensional Rheometer (FiSER) type devices, as schematized in Fig. 1(a).[23,41–45] Here, a fluid sample is contained between two circular endplates (diameter D_0, initial separation L_0) that are subsequently moved apart at an exponentially increasing rate such that $L(t) = L_0 \exp(\dot{\varepsilon}t)$, thus defining the imposed strain rate, $\dot{\varepsilon}$. The diameter of the resulting fluid filament is measured as a function of time ($D(t)$) and one of the endplates is connected with a force transducer in order to simultaneously measure the tension ($F(t)$), and hence the stress, see Fig. 1(b). The instantaneous Hencky strain is given by $\varepsilon_H = \ln[L(t)/L_0] = 2\ln[D_0/D(t)]$. These devices have been hugely successful at measuring transient extensional viscosities of fluids in almost ideal uniaxial extensional flow. However, due to a combination of the limit on the maximum velocity at which the endplate motors can run and the distance over which they can be physically separated, such devices are quite limited in both the range of strain rates and the total strain that can be applied. For these reasons, filament stretching rheometers are only really suited for testing fluids with rather long relaxation times $\lambda \sim O(1 - 100\,\mathrm{s})$. In addition, fluids must be quite viscous (typically $\eta > 10$ Pa s) so that gravitational sagging of the filament can be neglected at low strains before the onset of strain hardening.[44] At high strains or strain rates, endplate instabilities are problematic[46] and the free surface poses additional problems including bead-on-string instabilities,[47] evaporation in the case of volatile solvents, and adsorption of surface active species that can stabilize filaments to break up.[48]

A commercially available variant of the filament stretching rheometer is the Capillary Breakup Extensional Rheometer or CaBER device, Fig. 1(c).[49,50] This device is essentially based on a controlled "finger stretch" test and at this time is probably the most well-known and widely used of all extensional flow devices. Here, as with the FiSER, a cylindrical fluid sample is contained by surface tension between a pair of circular end plates (diameter D_0) with initial separation L_0. Unlike the FiSER, however, the sample is not stretched by a prolonged separation of the plates. In the case of the CaBER, the plates are only moved apart by a relatively small distance to reach a final separation L_f. At the final position L_f, the two plates are sufficiently far apart that capillary forces act to drive the fluid to separate into two hemispherical droplets. Uniaxial extensional flow is generated as the fluid neck thins down between the two endplates. For Newtonian fluids, it has been shown that the hour-glass-shaped fluid neck thins linearly with time at a viscosity-dependent rate.[51] For a complex fluids, such as polymer solutions, extra elastic stresses generated as the microstructure deforms retard the thinning process, resulting in an "elasto-capillary" thinning regime.[50] Here, a long and slender cylindrical fluid filament develops between the endplates and the filament thins exponentially with time. Using a

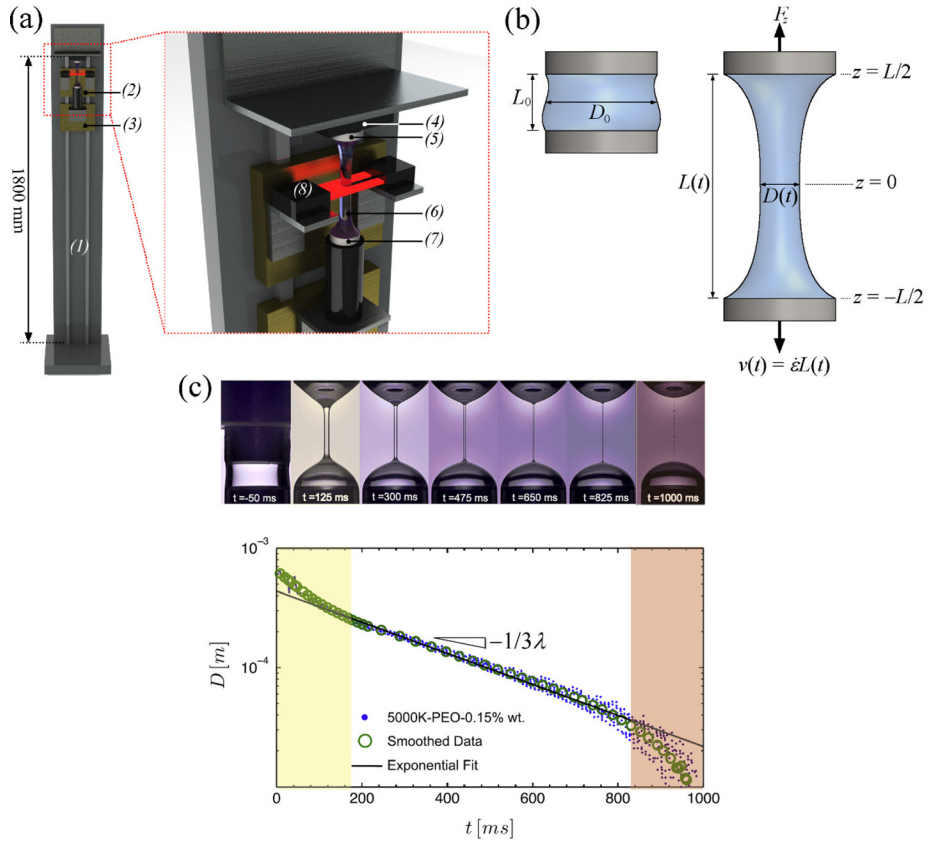

FIG. 1. Examples of extensional rheometric techniques by measuring the thinning of fluid filaments: (a) Schematic drawing of a FiSER device, consisting of: (1) linear stage, (2) and (3) traveling linear motors, (4) force transducer, (5) top end-plate, (6) fluid filament, (7) bottom end-plate, and (8) laser micrometer. (b) Parametric description of the stretching fluid filament in the FiSER. (c) Example data from a capillary thinning (CaBER) measurement, showing mid-filament diameter as a function of time for a semidilute poly(ethylene oxide) solution contained in a viscous solvent. The characteristic relaxation time λ can be found from the slope of the exponential decay within the elasto-capillary regime indicated by the central white region of the plot. Reprinted with permission from Keshavarz *et al.*, J. Non-Newtonian Fluid Mech. **222**, 171 (2015). Copyright 2015 Elsevier.

laser micrometer or video camera, the diameter of the fluid filament $D(t)$ is monitored as a function of time at the midpoint between the endplates (where pure uniaxial extension is best approximated), and this information is used to back out the extensional rate $\dot{\varepsilon} = -(2/D(t)) \cdot [dD(t)/dt]$ and accumulated Hencky strain $\varepsilon_H = 2\ln[D_0/D(t)]$. The rate of exponential decay of the filament diameter can be used to extract a relaxation time for the fluid.[49,50] In addition, assuming a balance between elastic and capillary forces, a measure of the transient extensional viscosity as a function of the strain can be obtained. The CaBER device is a compact and simple-to-use device that is useful in quality control applications and is also a very convenient laboratory tool for a quick assessment of the extensional properties of fluids. The CaBER device shares many features with the FiSER apparatus and shares the same advantages and disadvantages associated with the free-surface and asymmetry due to gravitational effects.[52,53] It is able to access fluids with rather lower viscosities and relaxation times than the FiSER: although in normal operating mode it is still restricted to fluids with relaxation times of several milliseconds and viscosities of several mPa s,[54] separating the CaBER endplates using the Slow Retraction Method (SRM) can probe even more weakly viscoelastic samples while avoiding inertia-induced oscillations of the fluid.[55] In addition, several techniques have been developed for generating liquid bridges and measuring capillary-driven filament thinning of microlitre fluid samples, which effectively obviate gravitational and inertial effects entirely.[27,56–59] Many of the aforementioned techniques have recently been reviewed in detail by Galindo-Rosales *et al.*[60] A recently developed related

technique that can probe extremely low viscosity and low elasticity fluids is Rayleigh-Ohnesorge Jetting Extensional Rheometry (ROJER), in which thinning sections of an unstable fluid jet during breakup are observed.[61,62] In CaBER-type techniques, if the elasto-capillary thinning regime is of sufficient duration, then the fluid strain can be sufficient for the extensional viscosity to reach steady state. However, probably the most important problems with capillary thinning-based techniques in general are: (1) the correct identification of the elasto-capillary regime can sometimes be difficult,[63] thus leading to concern about the validity of measurements; (2) the fluid column thins at a self-determined rate governed by its own particular properties (viscosity, relaxation time, and surface tension). It can be shown that in the elasto-capillary thinning regime (where properties of viscoelastic fluids can be derived), the Weissenberg number should be a constant $\mathrm{Wi} = 2/3$.[49,50] It is not possible to impose a controlled deformation rate to a fluid sample by using capillarity-driven thinning.

B. Flow through contractions and expansions

Over many years, much research has been conducted into viscoelastic extensional flows generated in contraction and expansion type geometries.[64–71] In flow through a contraction-expansion geometry, the fluid experiences a positive streamwise velocity gradient as it approaches and traverses the contraction plane and a negative streamwise velocity gradient as it enters an expansion.[72] Contraction geometries, both axisymmetric and planar, have long been of interest in the complex fluids community owing to their ability to generate strong extensional flows, their perceived potential to serve as simple extensional rheometers, and to the great variety of nonlinear instabilities that can be observed.[67,68,70,73–78] Although axisymmetric extensional flows are stronger than planar extensional flows (for a given extension rate),[71,74] planar flows are generally preferred experimentally due to the relative ease of performing flow visualizations. The contraction geometry is representative of a class of flows encountered widely in natural and industrial settings and the planar 4:1 abrupt contraction is considered as a benchmark problem for viscoelastic fluids in strong flows.[1,73,79] This is because numerical simulations (though challenging, especially at high Wi) are relatively straightforward compared with stagnation flows, allowing more ready comparison between experiment, simulation, and theory though testing of constitutive models.[79–82] For the same reasons, contraction and expansion flows have remained of significant interest in the era of microfluidics, which owing to the small characteristic length scales allow nonlinear dynamics to be accessed in regimes of large deformation rates (high Wi) and low inertia (low Re) that were unattainable in earlier macroscale pipe flows.[83–87]

Although a contraction geometry provides only a transient elongational flow while fluid elements travel through the contraction, the nominal extensional deformation rate $\dot{\varepsilon}$ is readily controlled via the volumetric flow rate through the contraction.[72,88] The applied fluid strain ε is effectively constant for a given device and is approximated by the contraction ratio (i.e., the ratio of upstream to downstream channel cross-sectional area).[74] Flows of viscoelastic polymer solutions through planar abrupt microfluidic contractions have been quite widely studied experimentally using streak imaging, velocimetry, pressure loss, and flow-induced birefringence (FIB) measurements.[83,84,86–90] These generally show a sequence of instabilities that develop with increasing flow rates or Wi, beginning with the observation of diverging streamlines upstream of the contraction plane and proceeding through to the development of lip vortices at the reentrant corners, then upstream vortices in the salient corners which grow in size as the Wi is further increased. At higher Wi, time-dependent and three-dimensional (3D) flow instabilities are observed, see Fig. 2(a). The exact onset conditions and nature of this progression of flow instabilities are highly dependent on the fluid properties, particularly the elasticity number of the fluid $\mathrm{El} = \mathrm{Wi}/\mathrm{Re}$,[83,84] and details of the flow geometry, i.e., contraction ratio, aspect ratio, and downstream length of the contraction.[85,91,92] Apart from only applying a fixed fluid strain, planar abrupt contractions suffer from several addition drawbacks as extensional rheometers. First, even for creeping Newtonian flows, the strain rate along the center line of the channel is not constant for a given imposed flow rate. Further, with viscoelastic fluids, the growth of vortices in the region upstream of the contraction plane causes even more severe consequences on the

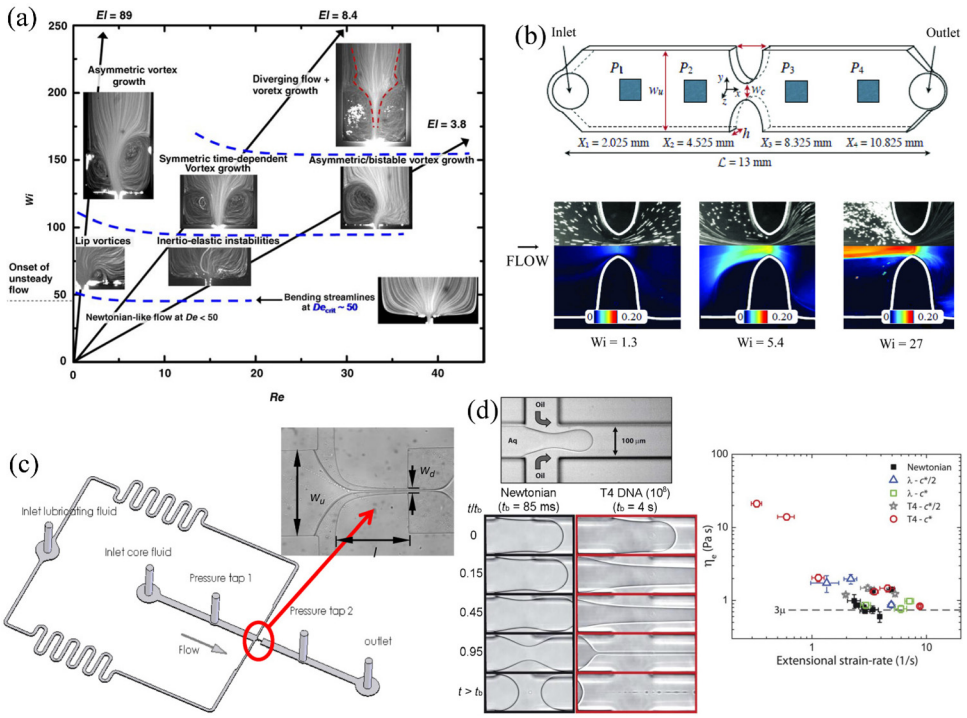

FIG. 2. Examples of devices for producing transient elongational flows in microfluidic devices: (a) Flows of aqueous poly(ethylene oxide) solutions through a microfluidic planar abrupt contraction geometry. Fluids with different shear viscosities and relaxation times have different elasticity numbers and follow different trajectories through Wi-Re parameter space, defining stability boundaries for the onset of vortices upstream of the contraction plane. Reprinted from with permission from Rodd *et al*., J. Non-Newtonian Fluid Mech. **129**, 1 (2005). Copyright 2005 Elsevier. (b) Schematic diagram of a hyperbolic contraction geometry with integrated MEMS pressure sensors, used as an extensional viscosity indexer and (below) combined streak imaging and flow-induced birefringence measurements made on a wormlike micellar solution in the hyperbolic contraction. Adapted with permission from Ober *et al*., Rheol. Acta **52**, 529 (2013). Copyright 2013 Springer Science + Business Media. (c) Schematic drawing of a lubricated microfluidic hyperbolic contraction incorporating pressure taps up- and downstream. The inset image shows a viscous Newtonian fluid entering the contraction from the left and lubricated by water entering from the top and bottom lateral inlets. Reprinted with permission from J. Wang and D. F. James, J. Rheol. **55**, 6103 (2011). Copyright 2011 The Society of Rheology. (d) (top) Illustration of the experimental setup for filament formation in a cross-slot microchannel and (below) examples of filaments formed by a Newtonian fluid and a DNA suspension at different fractions of the final filament breakup time t_b. The plot to the right shows the extensional viscosity of various fluids determined by the technique. Adapted with permission from G. Juarez and P. E. Arratia, Soft Matter **7**, 9444 (2011). Copyright 2011 The Royal Society of Chemistry.

flow field, meaning that the actual extension rate applied to fluid elements may be significantly, and unpredictably, modified compared with expectations. In addition, although pressure loss measurements for viscoelastic fluids may show a clear non-linearity due to the extra elastic stresses associated with microstructural deformation, it is very difficult to extract the purely extensional component from the bulk measurement without making some significant assumptions and approximations.[86,93]

Hyperbolic contractions (Fig. 2(b)) have been predicted to impose a nominally constant extension rate along the centerline without the generation of upstream vortices.[72,78] However, experiments with viscoelastic fluids in hyperbolic contractions have shown that this is unfortunately not the case.[10,94,95]

Ober *et al*.[95] studied a range of complex fluids (including viscoelastic polymer solutions, wormlike micellar solutions, and consumer products) in flow through a hyperbolic contraction using flow visualization, birefringence, and pressure measurements. The etched glass microdevice used by Ober *et al*.[95] is illustrated in Fig. 2(b). The device includes four flush-mounted MEMS pressure sensors in order to measure the pressure losses upstream of, downstream of, and across the contraction. The wormlike micellar solution used in that work was a shear-banding fluid composed of 100 mM cetylpyridinium chloride (CPyCl) and 60 mM sodium

salicylate (NaSal). Ober *et al*. argued that the effective lubrication layers present at the channel walls (formed due to shear localization of of the fluid) should result in a plug-like flow in the bulk and be beneficial for the generation of a more homogeneous extensional flow field through the contraction region.[95] However, at large enough Weissenberg numbers, i.e., sufficient to cause microstructural reorganization (as evidenced by birefringence measurements), large and almost stagnant vortical regions developed upstream of the contraction throat, and micelle orientation was clearly localized into a central band along the flow axis through the contraction (see streak images and birefringence visualization in Fig. 2(b)). Although such perturbations to the flow field are clearly undesirable for the purposes of performing "true" extensional rheometry, Ober *et al*. demonstrated how careful pressure measurements could enable such a device to be used as an effective *indexer* for the transient extensional viscosity of complex fluids.[95]

Wang and James[96] used flow in a microfluidic hyperbolic contraction which included side channels through which a lubricating fluid was introduced, see Fig. 2(c). Miscible lubricant fluids were found to completely encapsulate the core fluid, whereas immiscible lubricants were found to flow only along the side walls of the microchannel. Immiscible lubricants were thus preferred since they generated an almost shear-free plug flow in the core test fluid that was subjected to planar elongation through the hyperbolic contraction. Calculations were made to quantify the pressure drop arising from shearing at the core-lubricant interface and the top and bottom surfaces of the microchannel. This was subtracted from the total measured pressure drop in order to quantify elastic stresses and compute the extensional viscosity of dilute aqueous polymer solutions. The approach shows some promise, though care must be exercised since the results are highly dependent on the flow rate ratios between the core and lubricating fluids. In many cases, the core fluid does not follow the hyperbolic contours of the flow geometry, with the lubricating layer impinging into the region upstream of the contraction and filling the areas normally occupied by recirculating upstream vortices (which would be present in the case of a single phase flow without lubricant). In this case, the extension rate needs to be estimated from measurements of the thinning of the core fluid as a function of the distance along the channel and is found to be rather inhomogeneous. The ratio of flow rates between the core fluid and the lubricant may also affect the degree of shearing at the fluid-fluid interface, thus influencing the degree of polymer stretching and also the relative contributions to the total pressure drop.[96]

Arratia and coworkers[97–99] used a cross-shaped microchannel with three entry ports and one exit in order to form filaments of Newtonian and viscoelastic test fluids, see Fig. 2(d). The test fluid was injected into one of the entry ports and an immiscible sheath fluid was injected into two orthogonal entry ports, thus focussing the test fluid into a thinning filament within the outlet channel. The result is similar to a combination of the lubricated contraction experiment of Wang and James[96] and a capillary thinning or CaBER experiment, except the filament is planar, not uniaxial as in the CaBER device. As with a CaBER experiment, the filament width is measured as a function of time in order to compute the extension rate. Measurements at various locations along the filament showed reasonable homogeneity of the planar elongational flow over an extended period of time. By controlling the flow rate of the lubricating sheath fluid, the experiment of Arratia *et al*. allows some variation of the exponential rate of filament thinning, from which the steady extensional viscosity can be estimated. This interesting approach shows some promise and has so far been tested with Newtonian fluids and dilute aqueous poly(acrylamide) (PAA) solutions over a range molecular weight,[97,98] and also with DNA solutions.[99] Interestingly, while PAA solutions showed extensional thickening with increasing strain rate, some DNA solutions showed significant extension thinning (Fig. 2(d)), an effect which is not predicted theoretically[100] and is still not well understood.

C. Stagnation point flows

A well established method to apply a persistent extensional flow to a fluid element, required to achieve a steady state deformation of the microstructure at a given elongation rate, is achieved by having a continuous flow that incorporates a stagnation point. At a stagnation point, the strain rate is finite but the local flow velocity is zero. Hence, fluid elements become

trapped in the velocity gradient at the stagnation point for an undefined length of time and arbitrarily high fluid strains can accumulate. Fluid elements that pass through the region surrounding the stagnation point are still subjected to a velocity gradient, but for a finite time period and therefore accumulate a limited strain, which can still be very high, but which depends on the flow path line. The spatial distribution of fluid strain through the cross-slots is discussed further in Section IV B. A number of devices have been developed for the generation of idealized flow fields incorporating isolated stationary stagnation points that can be studied in the laboratory. The first of these was Taylor's 4-roll mill[101] for the study of the deformation and breakup of liquid drops, as schematized in Fig. 3(a). During the 1970s and 1980s, the four-roll mill was utilized extensively, along with the opposed jets apparatus (Fig. 3(b)), for the study of macromolecular dynamics of polymer molecules (and associated viscoelastic effects) in extensional flows using FIB measurements.[17,102–104] While the 4-roll mill is capable of producing a very good approximation to a purely planar extensional flow field with a stagnation point, the mechanically driven rollers are quite large with diameters on the centimeter scale. A significant volume of fluid $\sim O(1\,\mathrm{l})$ is required to immerse the system and inertia can become high at rather moderate extension rates, leading to flow instabilities.[105] More recently, microfluidic analogues of the 4-roll mill have also been developed and demonstrated to produce stagnation point planar elongation along with other flow types (see right-hand panel in Fig. 3(a)).[106,107] These devices have been used for studies of the dynamics of vesicles[108] and of DNA tumbling[109] and have potential applications in exploring drop deformation behavior in mixed flows.[110–112] However, so far, they have not actually been configured for the purpose of performing extensional rheometry per se.

The opposed-jets device (illustrated schematically in (Fig. 3(b)), originally conceived and developed by Frank and coworkers[17,113] is capable of generating either a uniaxial extensional flow (with the jets in "sucking mode") or a biaxial extensional flow (in "blowing mode"). The device was originally configured as an extensional rheometer by measuring the pressure drop across the jets as a function of the elongation rate (controlled via the macroscopic flow rate).[114,115] However, the measurement was only ever considered as providing an extensional viscosity *index* since shear contributions to the pressure drop arising from flow within the jet nozzles could not be accurately quantified and had to be estimated from pressure drop measurements made with the pure solvent. Further development of the opposed-jets by Fuller and coworkers[103,116,117] resulted in the once commercially available Rheometrics RFX instrument, which used a pivoting jet and torque rebalancing transducer to maintain a constant jet separation and obtain a measurement of the tensile stress. This device was used throughout the 1990s for extensional measurements of various complex fluids.[118–121] While the RFX method obviated the contribution of shear stresses coming from flow within the connecting pipework, it was later shown that the stress measurement was nevertheless often dominated by inertia.[122] Additional drawbacks of the apparatus include the inability to observe the flow field (leading to uncertainty in the assumption of symmetry) and the rather large sample volumes that are required to immerse the jets ($>100\,\mathrm{ml}$).

Many of the drawbacks of the 4-roll mill and the opposed-jets were overcome by the introduction of the cross-slots device by Scrivener *et al.*[123] for the study of drag reducing polymer solutions. The cross-slot device consists of mutually bisecting orthogonal rectangular channels, as shown in Fig. 3(c). Flow enters through two oppositely facing inlets and exits through the diametrically opposed pair of outlets. Assuming symmetry of the flow field, a stagnation point is formed at the exact center of the cross-over region and fluid is stretched in the vorticity and shear-free flow along the outlet axis.

The cross-slot device has several advantages over alternative apparatus for the purposes of extensional rheometry: (1) the flow is planar, which facilitates the use of optical techniques such as fluorescence imaging, birefringence measurement, and velocimetry; (2) the flow is bounded on both the inlets and the outlets, which aids in maintaining flow stability up to higher flow rates; (3) there is no air interface, which is attractive for biological samples containing surface-active species, and also eliminates evaporation of volatile solvents; (4) the applied strain rate is easily controlled via the macroscopic flow rate through the device; and (5) the

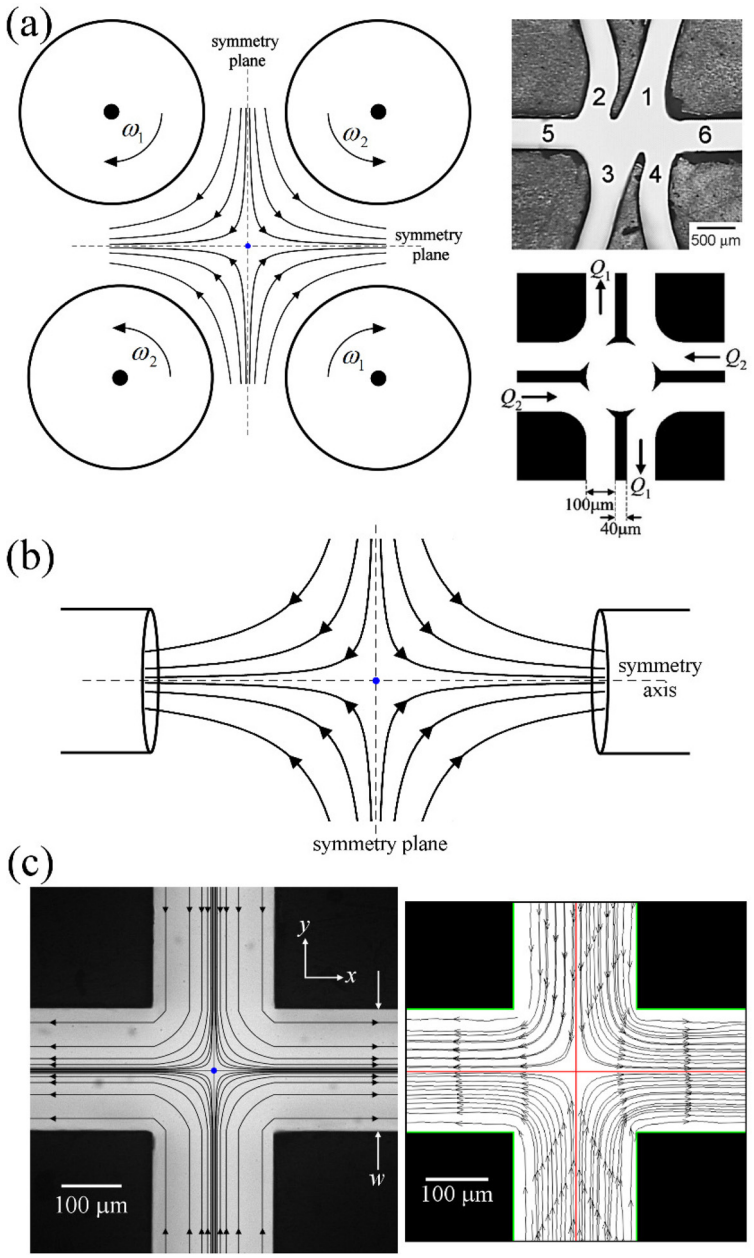

FIG. 3. Examples of devices for producing stagnation point elongational flows: (a) Schematic drawing of a four-roll mill device. If $\omega_2 = -\omega_1$, an approximation to pure planar elongation flow is generated. Images to right show examples of microfluidic four-roll mill analogues (Reprinted with permission from Hudson *et al.*, Appl. Phys. Lett. **85**, 335 (2004), Copyright 2004 AIP Publishing LLC and from Lee *et al.*, Appl. Phys. Lett. **90**, 074103 (2007). Copyright 2007 AIP Publishing LLC). (b) Schematic drawing of an opposed-jets apparatus in "sucking mode," which generates a uniaxial extensional flow along the symmetry axis. The jets can also be reversed into "blowing mode" in order to generate a biaxial extensional flow over the symmetry plane. (c) Light micrograph of a microfluidic cross-slot device ($w = 200\,\mu$m) to produce planar elongation. Superimposed streamlines were generated from the ideal streamfunction and indicate the direction of flow. (Right) Experimental streamlines measured in the midplane of same device using particle image velocimetry (PIV) on a Newtonian fluid seeded with fluorescent microparticles. The symmetry planes are indicated by the superimposed red lines. Reprinted with permission from S. J. Haward, Biopolymers **101**, 287 (2014). Copyright 2013 Wiley Periodicals, Inc.

extensional viscosity can be assessed by either applying the stress-optical rule to measurements of the birefringence[124–128] or measuring the bulk pressure drop (ΔP) across the device (a detailed discussion of this will be given in Section IV).

The cross-slot device is quite versatile, since it is readily scalable. Larger devices with typical channel width $w \sim O(1\text{–}10\,\text{mm})$ have been constructed that are suitable for extensional measurements with high viscosity elastic fluids such as polymer melts.[125,127,129,130] The simplicity of the cross-slots geometry also makes it amenable for fabrication at the microscale. The strain rate in the cross-slot scales with the inverse of the channel dimension ($\dot{\varepsilon} \approx 2U/w$, where U is the average flow velocity), while inertial effects, as quantified by the Reynolds number, scale linearly with the channel dimension ($\text{Re} = \rho U w/\eta$). By suitable reduction in length scale and appropriate driving of the flow, very high extension rates are achievable while keeping inertia low, meaning that microfluidic cross-slots can probe the elasticity of fluids with low shear viscosities and short relaxation times. In fact, the advantages of miniaturization were recognized early on in the development of the cross-slot by researchers at the University of Bristol, who were fabricating micro-scale devices (by hand) for the study of dilute polymer solutions at high Wi but low Re as early as the 1980s.[131–133] Miniaturization provides further benefits since smaller sample volumes are required, allowing investigations with exotic fluids and biological samples, for example.

III. USE OF THE CROSS-SLOTS IN MICROFLUIDIC EXPERIMENTS

We will define the cross-slot as having a channel width, w, depth, d, and aspect ratio, $\alpha = d/w$. As depicted in Fig. 3(c), in normal operating mode, fluid is injected into one pair of opposed channels (here shown vertically, along the y-direction) and is either withdrawn from or simply forced to exit, through the remaining pair of opposed channels (here horizontally, along the x-direction). The neutral direction through the depth of the device (normal to the xy plane) is defined as the z-direction. The origin of the reference system $x = y = z = 0$ is located at the geometric center of the device, which coincides with the stagnation point (provided that the flow is symmetric). Ideal planar elongation, which is approximated by flow in the cross-slot device, is described by a deformation rate tensor $\mathbf{D}$ with components given by $D_{xx} = \partial v_x/\partial x = \dot{\varepsilon}$ and $D_{yy} = \partial v_y/\partial y = -\dot{\varepsilon}$, and with all other components equal to zero.[33] The ideal streamfunction is described by $\psi = \dot{\varepsilon} xy$, which traces out hyperbolic streamlines with the stagnation point located at the singularity. The experimental streamlines shown to the right in Fig. 3(c) were measured at the midplane (i.e., the $z = 0$ plane) of a microfluidic cross-slot device with $w = 200\,\mu\text{m}$ and $d = 1\,\text{mm}$ (i.e., $\alpha = 5$) for a Newtonian fluid flowing at low Reynolds number. The ideal hyperbolic streamlines are clearly perturbed by the four reentrant corners; however, approaching the stagnation point the flow field approximates the ideal situation increasingly well. It has been shown from two-dimensional (2D, $\alpha = \infty$) fluid dynamics simulations that the elongation rate varies by less than 5% within a radius of $w/16$ around the stagnation point.[134] Flow velocimetry measurements made in the midplane of a lower aspect ratio ($\alpha = 0.53$) cross-slot device have shown reasonable agreement with expectations for planar elongational flow over a wider radius around the stagnation point of approximately $w/4$.[135] However, it is important to note that even in deep planar devices with high α, the flow only approximates to 2D. The no-slip boundary condition at the top and bottom surfaces will always result in some variation in the flow velocity (and hence the strain rate) through the channel depth. In addition, it has been found that at quite moderate Reynolds numbers ($20 \lesssim \text{Re} \lesssim 100$, depending on α), the flow around the corners of the cross-slot can result in the formation of Dean vortices[136] in the channel outlet and the onset of fully 3D flow instabilities.[137–141] Care must be taken to maintain the Reynolds number as low as possible in cross-slot flow experiments in order to maintain flow symmetry and stability and the best approximation to 2D planar flow. Flow instabilities resulting from fluid inertia (and elasticity) are discussed further in Section IV C.

Early experiments with polymer solutions in cross-slot devices showed the formation of highly localized birefringent strands extending downstream from the stagnation point, indicating the extension and alignment of polymer chains as the strain rate was increased beyond a critical value $\dot{\varepsilon}_c$ such that the Weissenberg number exceeded approximately 0.5–1.[17,131–133] The inverse of $\dot{\varepsilon}_c$ could thus be considered as the macromolecular relaxation time, and the molecular weight dependence of the relaxation time agreed well with the theoretical predictions.[133,142]

The birefringence signal reached saturation levels as the strain rate was increased, which was taken as evidence of polymer chains approaching full extension. Further evidence of this behavior came from the discovery that chains would undergo central scission.[133]

More recently, Chu and coworkers[19,35,143] used a microfluidic cross-slot in order to trap fluorescently labelled DNA at the stagnation point and watch individual molecules unravelling in real time. Fig. 4(a) shows several time-series of individual λ-DNA molecules with different initial conformations accumulating strain in the planar elongational flow field at $\dot{\varepsilon} > \dot{\varepsilon}_c$. Depending on the initial configuration and orientation relative to the flow direction, the molecules unravel at different rates and can become trapped in metastable kinked, folded, or knotted configurations. However, in general, after sufficient residence time in the extensional flow field, all molecules become highly aligned in the direction of the velocity gradient. Ensemble-averaged data showed that the macromolecular deformation became increasingly affine with the fluid strain as the Weisenberg number increased.[35] The ensemble-average steady-state stretch approached around 80% of the DNA contour length at very high deformation rates. Later, Schroeder *et al.*[143] confirmed the coil-stretch relaxation time hysteresis predicted by De Gennes.[16] A detailed review of these studies has been provided by Shaqfeh.[144] Rather similar experiments have also been conducted showing the deformation and orientation of individual wormlike micelles, also for $\mathrm{Wi} > 0.5$.[145]

Dylla-Spears *et al.*[134] have shown how the extension of DNA in cross-slot microchannels can be used for accurate single-molecule sequence detection using fluorescence imaging. Xu and Muller[146] demonstrated the detection of sequence-specific DNA-bound enzymes via cleavage of the linearized DNA trapped hydrodynamically at the stagnation point, as reproduced in Fig. 4(b). In the works of both Dylla-Spears[134] and Xu and Muller,[146] DNA was trapped by manipulating the flow rate in one of the two exit channels via manual control of the hydrostatic pressure head. Schroeder and coworkers[147–151] have developed a more advanced system of active feedback between real-time flow visualization at the stagnation point and control of the flow rates through each channel of the cross-slot using microfluidic valves in order to achieve extremely precise hydrodynamic trapping, control, and manipulation of particles and cells (see Fig. 4(c)). The approach holds the promise to significantly enhance the ability to observe the effects of the extensional flow field at the stagnation point on the deformation of microscopic structures over much extended residence time durations. Very recently, Toh *et al.*[152] have shown similar control over the location of the stagnation point in a modified cross-slot device in which confined and well-controlled chemical gradients can be generated. The device shows promise for the study of hierarchical decision making processes that occur during intercellular communication of bacteria and neutrophils and of cell chemotaxis.

Nève *et al.*[153] have used optical tweezers in order to trap live single osteoblast and myoblast cells at the stagnation point of a cross-slot device and to observe their deformation as a function of the imposed extensional rate. Recently, there has been growing interest in the potential of using microfluidic cross-slots to perform single cell phenotyping based on cell deformability at the stagnation point.[154–157] Di Carlo and coworkers[154,156] have used inertial flow focussing to align single cells on the inlet axis of a microfluidic cross-slot device with very small dimensions ($w = 68\,\mu$m, $d = 28\,\mu$m) in which strain rates $\dot{\varepsilon} > 10^5\ \mathrm{s}^{-1}$ could be reached. The deformation of the cells as they passed through the stagnation point was imaged at high speed and used to perform mechanical phenotyping at high throughput (2000 cells per second). Differences in the deformabilities of cells found in pleural fluids could potentially diagnose a range of conditions including various cancers.[154,156] Cha *et al.*[155] performed similar experiments on Red Blood Cells (RBC's) and human Mesenchymal Stem Cells (hMSC's), but used viscoelastic flow focussing[158] to guide the cells into the stagnation point. The deformability of hMSC's was found to vary depending on the state of nutrient starvation and may be used as an indicator of cell quality or health, while the deformability of RBC's may be used as a diagnostic for various pathophysiological conditions including malaria and diabetes.[155,157] It is also important to mention very recent work examining the deformation of bio-microcapsules formed from human Serum Albumin (hSA).[159] An interesting experimental design allowed the capsules to be viewed at the stagnation point from both above (in the *xy* plane) and from the side

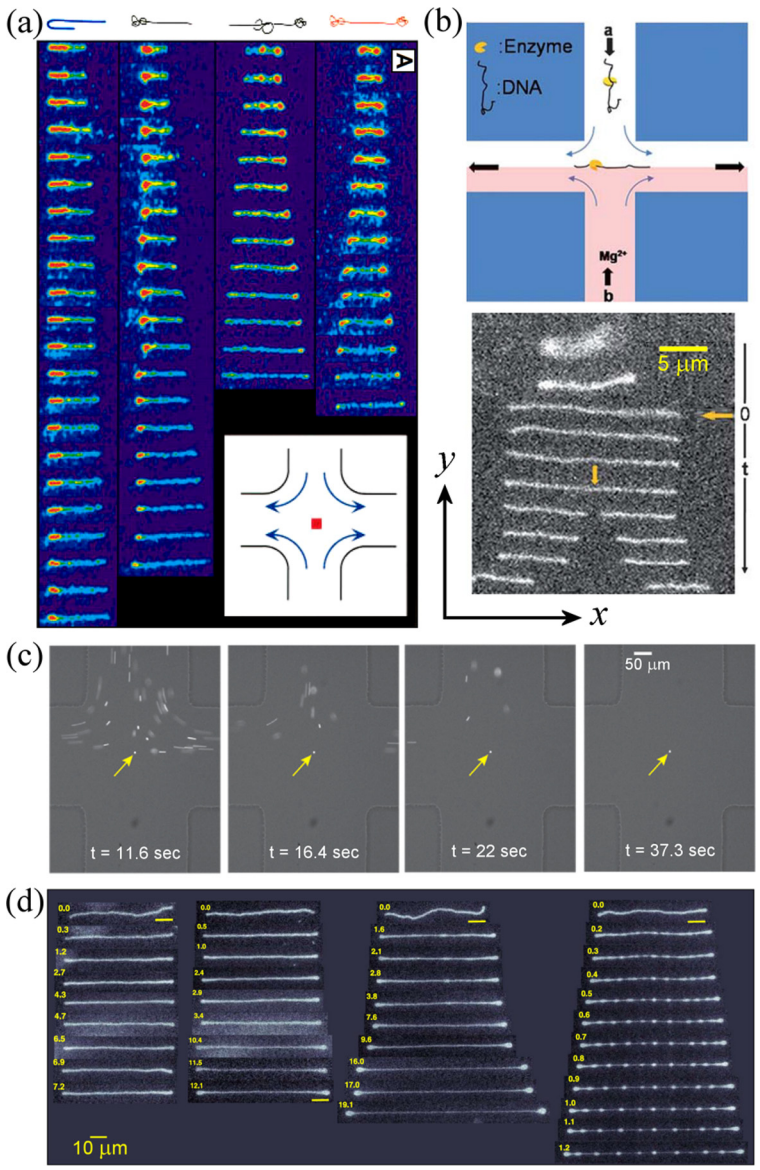

FIG. 4. Examples of the use of stagnation point extensional flow in microfluidic cross-slot devices: (a) Accumulation of strain in individual DNA molecules held at the stagnation point. Panels show (left-right) DNA molecules in folded, half-dumbbell, knotted, and dumbbell conformations unravelling over time (top-bottom). Reprinted with permission from Perkins *et al*., Science **276**, 2016 (1997). Copyright 1997 AAAS. (b) Enzyme-bound DNA (injected through channel "a") stretching at the stagnation point and being cleaved at the binding site by the addition of Mg^{2+} ions that are injected through channel "b." Reproduced with permission from W. Xu and S. J. Muller, Lab Chip **11**, 435 (2011). Copyright 2011 The Royal Society of Chemistry. (c) Hydrodynamic trapping of a 2.2 μm diameter particle at the stagnation point. (left-right) The particle is initially isolated from a group and held at the stagnation point as the remainder are advected away by the flow over the subsequent 25 s period. Reprinted with permission from M. Tanyeri and C. M. Schroeder, Nano Lett. **13**, 2357 (2013). Copyright 2013 American Chemical Society. (d) Stretching of tubular vesicles at the stagnation point at different strain rates: $(1-r)\,\dot{\varepsilon} = 0.09\ s^{-1}$, $0.14\,s^{-1}$ (showing dumbbell instability), $0.19\ s^{-1}$, and $0.92\,s^{-1}$ (showing pearling instability). Yellow numbers indicate accumulated fluid strain, $\varepsilon = \dot{\varepsilon}t$. Reprinted with permission from Kantsler *et al*., Phys. Rev. Lett. **101**, 048101 (2008). Copyright 2008 The American Physical Society.

(*xz* plane), and the capsules were observed to deform into discus-like ellipsoids. Measurements of the axial deformation with the applied strain rate (prior to capsule bursting) enabled the calculation of the Poisson ratio of the hSA membrane. Kantsler *et al.*[160] made observations of giant vesicle dynamics at the stagnation point, reporting the appearance of a wrinkling instability subsequent to a sudden switch in direction of the extensional flow field. In another work, by

stretching of tubular vesicles in the cross-slots, Kantsler *et al.*[161] observed significantly non-affine vesicle deformation and instabilities characterized by dumbbell and "string of pearls" formation as the strain rate was increased (Fig. 4(d)). A slowing-down of the dynamics of the vesicle extension close to the critical transition to dumbbell formation was interpreted as being due to the large number of configurational states available to the vesicle when entropic elasticity is balanced by the hydrodynamic stretching force.

IV. EXTENSIONAL RHEOMETRY USING MICROFLUIDIC CROSS-SLOTS

As discussed above, cross-slot devices have many qualities suggesting their suitability as extensional rheometers. To briefly summarize, the flow near the stagnation point approximates pure planar elongational flow and the flow along the symmetry axes is shear and vorticity free. Arbitrarily high fluid strains are applicable, and the imposed strain rate is easily controlled by manipulation of the volume flow rate. In addition, high aspect ratios ensure that the strain rate is nominally uniform through the neutral z-direction. The planar nature of the device also makes it amenable to the use of optical probes such as fluorescence imaging and flow velocimetry, which allows confirmation of the symmetry and stability of the imposed flow field. Flow birefringence measurements may also be made in order to register the deformation of any microstructure,[162] and in certain cases, directly assess the stress field.[124] Devices have also been made suitable for x-ray and small angle neutron scattering studies.[163,164] The use of microfluidic scale cross-slot devices allows access to high strain rates for low inertia so that elastic effects can be probed in samples with low shear viscosities and short relaxation times and by means of small sample volumes. Additionally, samples are completely enclosed in the clean, inert environment inside the geometry, eliminating surface tension and gravitational effects, and evaporation of volatile samples. Also, there is no air interface, so measurements are not affected by surface film formation by hydrophobic species.[48,165,166] All of these characteristics make the cross-slot device a suitable candidate for testing biological samples.

Extensional rheometry can be performed in the cross-slots by making measurements of the bulk pressure drop across an inlet and an outlet. The most effective approach is to make two measurements of the pressure drop for each imposed average flow velocity, U, see Fig. 5. First, the pressure is measured with flow through all four channels in order to obtain $\Delta P_{total}(U)$, which contains pressure contributions from shear at the channel walls and extension along the flow axis. A second measurement is made for flow around one corner of the device in order to obtain $\Delta P_{shear}(U)$, which approximates the shearing contributions to ΔP_{total}. A subtraction between these two quantities enables the estimation of the excess pressure drop due to the extensional component in the stagnation point flow field $\Delta P_{excess}(U)$, which can be related to the tensile stress difference $\Delta\tau(U)$

$$\Delta\tau(U) \propto \Delta P_{excess}(U) = \Delta P_{total}(U) - \Delta P_{shear}(U). \tag{1}$$

A strain rate-dependent apparent extensional viscosity can then be computed according to[24]

$$\eta_{E,app}(\dot{\varepsilon}) = \frac{\Delta\tau(\dot{\varepsilon})}{\dot{\varepsilon}}, \tag{2}$$

where $\dot{\varepsilon} \approx 2U/w$.

Such a straightforward and direct quantification of the extensional stress component as described by Eq. (1) has not been achieved in other fluidic geometries involving stagnation point or transient extensional flows, where significant assumptions and approximations must generally be made in order to remove stress contributions due to shear.[73,86,93,95,122]

A local value for the principal stress difference $\Delta\tau$ can also be estimated from measurements of the flow-induced birefringence and applying the stress-optical rule.[124,167] The stress-optical rule states that, for limited deformations of the microstructure, the tensile stress-difference is directly proportional to the birefringence, Δn

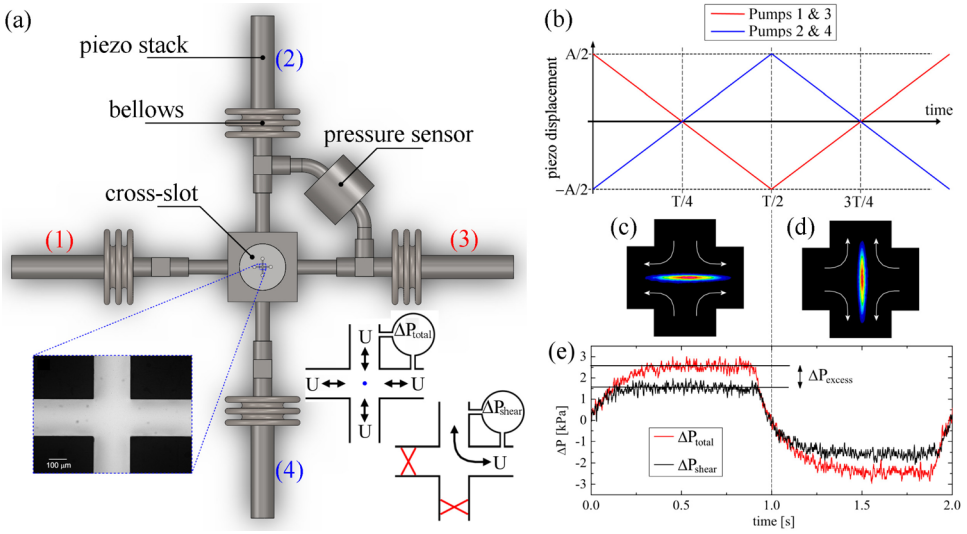

FIG. 5. Extensional Flow Oscillatory Rheometry (EFOR): (a) Schematic representation of the EFOR apparatus, with piezo-actuated micropumps on all four inlet-outlets. Detail to bottom left shows a cross-slot with $w = 200\,\mu$m, $d = 1$ mm ($\alpha = 5$). Inset to bottom right illustrates the two measurements of the pressure drop required to extract the extensional stress difference, $\Delta\tau$. (b) Graphical representation of the piezo pump displacement applied in order to obtain a constant volume flow rate over each half-cycle period, $T/2$. (c) and (d) False color birefringent strands observed in the cross-slot for flow of a 0.03 wt. % solution of 10.2 MDa a-PS in DOP during the first and second half cycles of the piezo pumps, respectively. The conditions applied to the piezos are $A = 50\,\mu$m, $T = 2$ s, providing a strain rate of $\dot{\varepsilon} = 1025\ \text{s}^{-1}$ and $\text{Wi} \approx 6$. (e) Pressure drop measured over one pump cycle under the same conditions as part ((c) and (d)).

$$\Delta\tau(\dot{\varepsilon}) = \frac{\Delta n(\dot{\varepsilon})}{C}, \tag{3}$$

where the constant of proportionality, C, is called the stress-optical coefficient. Hence, from birefringence measurements made in the vicinity of the stagnation point, a local extensional viscosity can be computed according to

$$\eta_E(\dot{\varepsilon}) = \frac{\Delta n(\dot{\varepsilon})}{C\dot{\varepsilon}}. \tag{4}$$

From inspection of Eqs. (1)–(4), it is apparent that if the two measures of the extensional viscosity are to be consistent, then a plot of Δn vs ΔP_{excess} should yield a straight line with gradient equal to the stress optical coefficient C. This relationship has been shown to hold up to surprisingly high strains for a variety of fluids including dilute and semi-dilute solutions of flexible and semiflexible polymers and also shear thinning wormlike micellar solutions.[61,126,128] However, the linear relationship has been observed to break down for shear banding wormlike micelles[128] and for human saliva,[126] in which the MUC5B mucins form a complex proteinaceous network structure that can rupture as the strain rate is increased.[126,168]

Birefringence measurements as a function of the strain rate also enable the assessment of the relaxation time, λ, of the fluid microstructure on the basis that optical anisotropy will arise for $\text{Wi} = \lambda\dot{\varepsilon} > 0.5$. Furthermore, for dilute solutions of polydisperse polymers, it has been shown that the Δn *versus* $\dot{\varepsilon}$ curve can be considered as a cumulative molecular weight distribution; as the strain rate is increased, progressively shorter molecules (i.e., shorter relaxation times) in the molecular weight distribution stretch and contribute to the measured birefringence. If the relationship between molecular weight and coil-stretch relaxation time for the polymer is known (or can be determined), then the molecular weight distribution can be computed from the birefringence.[15,126,133,169–171] The technique has been termed "hydrodynamic chromatography" and shows high sensitivity to high molecular weight tails of distributions (where Δn increases rapidly with $\dot{\varepsilon}$). High molecular weight tails are highly important rheologically and difficult to resolve using conventional techniques such as gel-permeation chromatography.[170]

A. Oscillatory extensional rheometry: The extensional flow oscillatory rheometer (EFOR)

The idea of performing extensional rheometry using an oscillatory flow within a stagnation point device was originally proposed and demonstrated by Odell and Carrington[170] and was further developed by Haward *et al.*[126,172,173] The principles behind the so-called EFOR are illustrated in Fig. 5. Briefly, the fluid sample is contained within the cross-slot device and four stainless-steel bellows that terminate each of the four arms of the cross. The bellows can be compressed or expanded by the displacement of pre-loaded piezo stacks that displace approximately linearly with the voltage applied across them (corrections can be made to the applied voltage in order to account for hysteresis in the piezo voltage-displacement loop). Providing that the total displacement of all four piezos at any instant in time is zero (thus conserving the volume of the sample fluid), arbitrary displacement profiles can be applied to the piezo stacks. In order to obtain a planar elongational flow with a constant strain rate, the bellows should be compressed or expanded at a constant rate, thus leading to a constant total volume flow rate through the cross-slot device. To achieve this, each piezo stack should be displaced with a triangular profile in phase with its opposing partner and 180° out of phase with the orthogonal pair of piezos, see Fig. 5(b). The displacement profiles of the piezo pumps are variable over a range of amplitude A and period T, which allow control of the strain rate thus

$$\dot{\varepsilon} \approx \frac{4a_{eff}A}{w^2 dT}, \tag{5}$$

where a_{eff} is the effective cross-sectional area of the bellows. The bellows used by Haward *et al.*[126,172,173] had $a_{eff} \approx 400$ mm^2, but it can be seen that significant flexibility in available strain rates is possible through the selection of bellows, the choice of piezo-stack operating range, and of course the dimensions of the cross-slot device itself.

The result of applying such a triangular pump profile to a dilute solution ($c = 0.03$ wt. %, $c/c^* \approx 0.1$) of a high molecular weight ($M_p = 10.2$ MDa), low polydispersity ($M_w/M_n = 1.17$) atactic polystyrene in a room temperature theta solvent dioctyl phthalate (a-PS in DOP) is illustrated by Figs. 5(c) and 5(d), which shows birefringence (indicating macromolecular orientation) aligned along the x-axis for the first pump half cycle and along the y-axis for the second pump half cycle. The corresponding pressure drops (ΔP_{shear} and ΔP_{total}) are shown in Fig. 5(e). It can be seen that the pressure drop reaches a steady value within each half cycle. This indicates that the flow has achieved steady state and that the microstructure has relaxed within the timescale of the flow. This can also be expressed by the Deborah number of the flow, which compares the relaxation time to the observation time of the experiment, $\mathrm{De} = \lambda/t_{obs}$. In the case illustrated in Fig. 5(e), $\lambda \approx 6.0$ ms and $t_{obs} = T/2 = 1$ s, thus $\mathrm{De} \ll 1$ suggesting the flow should be steady state.

The EFOR system has been well characterized using flow velocimetry, pressure drop, and flow birefringence measurements with Newtonian fluids and model polymer solutions.[126,170,172,173] Fig. 6 shows some data obtained with the same 0.03 wt. % a-PS solution presented in Figs. 5(c)–5(e). In Fig. 6(a), the birefringence (measured at the stagnation point, $x = y = 0$) and the excess pressure drop are presented as a function of the applied strain rate; both follow identical sigmoidal trends as $\dot{\varepsilon}$ is increased. When the two quantities are plotted against each other, a straight line through the origin is obtained (Fig. 6(a), inset). As indicated by Eqs. (1)–(4), the gradient of the straight line gives a value for the stress-optical coefficient of the polymer solution, here $C = -5.7 \times 10^{-9}$ Pa^{-1}.[126] This is in close agreement with the literature values obtained by accepted and established methods.[174–176] The use of the less noisy birefringence measurement to obtain the extensional viscosity according to Eq. (4) provides the curve shown in Fig. 6(b). Compared with the (constant) shear viscosity of the fluid ($\eta \approx 50$ mPa s), the Trouton ratio varies with the Weissenberg number as shown in the inset. As the Wi increases beyond 0.5, the extensional viscosity and Tr undergo a rapid increase, as expected. However, the curves do not increase monotonically, as would be expected from theoretical considerations,[177] but begin to decrease with $\mathrm{Wi} \gtrsim 1$. Such extensional thinning was also observed in the experiments

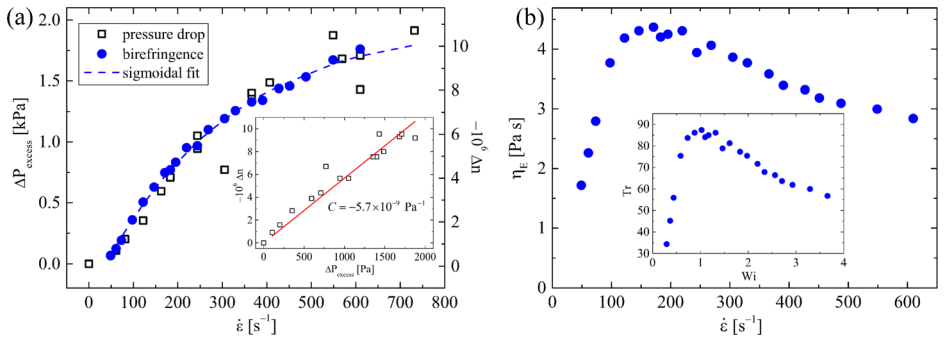

FIG. 6. EFOR with a 0.03 wt. % solution of 10.2 MDa a-PS in dioctyl phthalate: (a) Excess pressure drop and birefringence (measured at the stagnation point) as a function of the applied strain rate. The birefringence is well described by a sigmoidal function. Inset shows the birefringence as a function of the excess pressure, showing a linear relationship and yielding a stress-optical coefficient, C, for the fluid. Adapted with permission from Haward *et al.*, Soft Matter **7**, 9908 (2011). Copyright 2011 The Royal Society of Chemistry. (b) Extensional viscosity as a function of the strain rate in the cross-slot device for the same polymer solution shown in part (a) and, inset, Trouton ratio as a function of the Weissenberg number. For a Newtonian fluid in planar elongation flow, Tr = 4.[33]

of Arratia and Juarez[99] with DNA solutions. A possible explanation is the impedance of macromolecular strain accumulation at high deformation rates due to chains becoming trapped in metastable kinked or knotted states.[19,100]

A minor adaptation to the EFOR hardware involved the addition of a fluid injection point upstream of the central cross over region of the cross-slot device.[13,126] In this case, the pipework and bellows could be filled with pure solvent in order to act as a hydraulic fluid to drive the flow, while a small quantity of the test fluid was loaded only into the region of extensional flow around the stagnation point. By this method, data could be gathered using sample volumes of $\sim O(10\text{–}100\,\mu l)$ per test point, depending on driving parameters (A and T) imposed to the four micropumps. The system has been used to examine physiological fluids including human Whole Saliva (hWS) and porcine Synovial Fluid (pSF), see Fig. 7.[13,15,126,171] The ability to characterize the extensional properties of such fluids has been a long standing challenge and may lead to improved understanding of the development of conditions such as osteoarthritis, cystic fibrosis, oral mucositis, Sjögren's, and asthma, in which fluid rheology is drastically altered from its healthy state.[178–182] In addition, the characterization of biological fluid samples under extensional deformations should enable improved design and formulation of the prosthetic fluids that are used in the palliative treatment of many such conditions.

The EFOR system presents some interesting features compared with continuous flow systems. For example, fluid can be cycled repeatedly through the stagnation point while being maintained within the measurement region of the cross-slot, facilitating investigations of thermomechanical degradation of macromolecules. This feature has recently been employed to demonstrate mid-chain mechanical scission of Hyaluronic Acid (HA), a high molecular weight polysaccharide abundant in the synovial fluid, which becomes degraded during the progression of joint disease (see Fig. 8).[15,171,178,179] Moreover, it is apparent that for a given imposed pump profile parameters (A and T), the stretching along each orthogonal flow direction (x, y) is applied for a time $t = T/2$. We therefore have a system in which we have control of both the strain rate and the fluid strain accumulated at the stagnation point

$$\varepsilon = \dot{\varepsilon} t \approx \frac{2a_{eff}A}{w^2 d}. \tag{6}$$

Comparing Eqs. (5) and (6), it is clear that by fixing the piezo amplitude A constant and varying T, a strain rate sweep can be performed for a fixed value of the strain. By varying A and T in proportion with each other, the strain can be swept for a fixed strain rate. This feature of the device has yet to be fully investigated.

The EFOR is also an excellent platform for the study of transient extensional rheological effects and has been used to show apparent stress overshoots on flow startup,[172] buckling

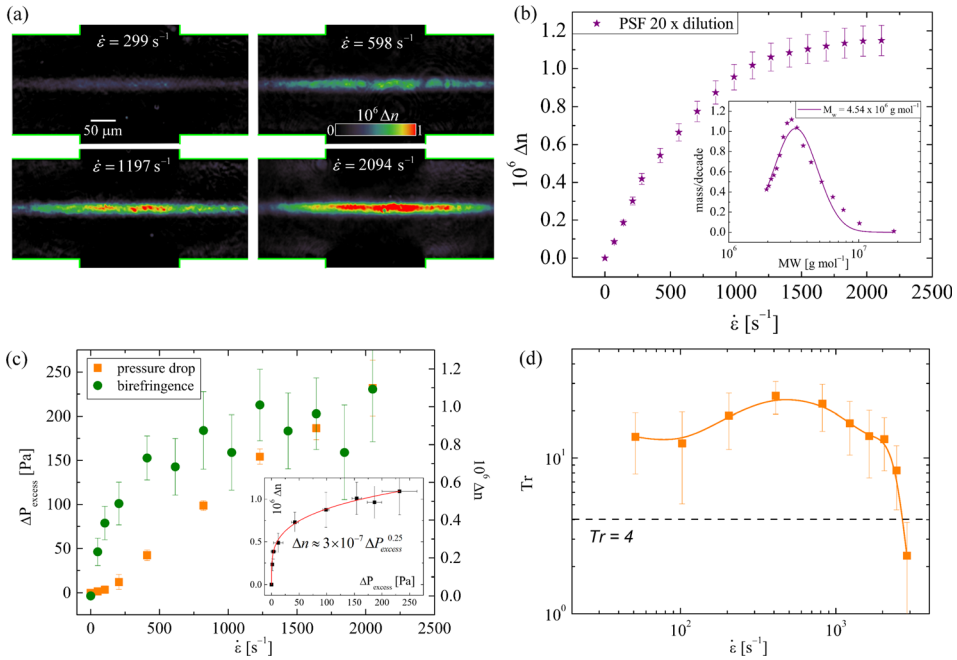

FIG. 7. Extensional Flow Oscillatory Rheometry with physiological biofluids: (a) Birefringence observed in the cross-slots for a sample of pSF at the imposed strain rates indicated on the images. Reprinted with permission from S. J. Haward, Biopolymers **101**, 287 (2014). Copyright 2013 Wiley Periodicals, Inc. (b) Birefringence (measured at the stagnation point) for a diluted pSF sample over a range of strain rates. Inset shows the molecular weight distribution derived from the birefringence measurement, fitted with a log-normal distribution function. Reprinted with permission from S. J. Haward, Biopolymers **101**, 287 (2014). Copyright 2013 Wiley Periodicals, Inc. (c) Birefringence and excess pressure drop measured for hWS in the cross-slots. In this case, the stress-optical coefficient, C, is not single valued because a power law relationship is observed between Δn and ΔP_{excess} (inset, red line). Adapted with permission from Haward *et al.*, Soft Matter **7**, 9908 (2011). Copyright 2011 The Royal Society of Chemistry. (d) Trouton ratio of hWS determined from the pressure measurements in part (c). The large reduction in Tr for strain rates $\dot{\varepsilon} \gtrsim 1000$ is attributed to breakup of the MUC5B mucin network. Adapted with permission from Haward *et al.*, Soft Matter **7**, 9908 (2011). Copyright 2011 The Royal Society of Chemistry.

instabilities of elastic strands during the transition in flow direction,[183] and slow relaxation of birefringence following the cessation of flow.[126,172] The latter two effects have been attributed to coil-stretch hysteresis of the flexible polymer that was employed in the experiments.[16]

Quite recently, a new system has been proposed for performing dynamic extensional rheometry by superimposing pulsations onto a continuous flow in a cross-slot micro-channel using

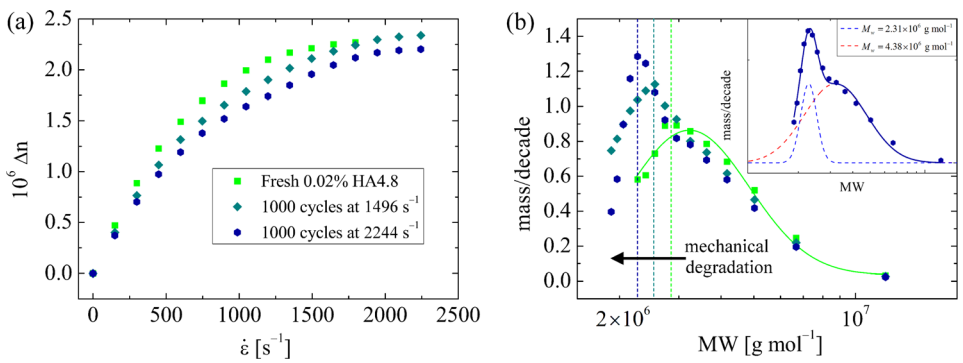

FIG. 8. Degradative effect of repeated cycling of a dilute solution of high molecular weight hyaluronic acid (nominal MW = 4.8 MDa) through the stagnation point. (a) Birefringence (measured at the stagnation point) for fresh fluid and after 1000 cycles at the indicated strain rates. (b) Molecular weight distributions derived from the data in part (a). The distribution for the fresh fluid is well-described by a single log-normal function. The distribution for the most degraded sample can be fitted by a sum of two log-normal functions, with peak molecular weight values that indicate chain halving. Reprinted with permission from S. J. Haward, Biopolymers **101**, 287 (2014). Copyright 2013 Wiley Periodicals, Inc.

a syringe pump and a reciprocal diaphragm pump connected in series.[184] The device has been characterized with Newtonian fluid and for various superposed waveforms using flow velocimetry methods, but so far no rheometric data have been presented using the system. Finally, we note that oscillatory flow in cross-slots has also been proposed as an effective method for performing active micro-mixing.[185,186]

B. Optimizing the cross-slots: The optimized shape cross-slot extensional rheometer (OSCER) geometry

A drawback of performing extensional rheometry using the standard type cross-slot geometry with square corners is that the flow field only approximates to the assumption of hyperbolicity quite close to the stagnation point.[134,135] Along the outlet flow axis, the strain rate has a maximum at the stagnation point and decays rapidly with distance along the outlet channels.[187] Alves[188] proposed a numerical scheme for optimizing the shapes of flow geometries in order to achieve specific desired flow characteristics and applied the method to the cross-slot with the aim of obtaining a homogeneous elongation rate over a wide region around the stagnation point spanning both the orthogonal flow axes. A 2D shape was optimized over a length of $L_{ext} = 15w$ and was predicted to provide a quasi-uniform strain rate $\dot{\varepsilon} = 0.2U/w$ (here, w is the channel width up- and downstream of the optimized region, as shown in Fig. 9(a)). A device was fabricated with a high aspect ratio ($d/w = 10$) in order to closely approximate the 2D configuration used for the optimization.[24] Characterization tests with Newtonian fluids for Re≲3 in the optimized device provided excellent agreement with the numerical predictions, as shown in Fig.

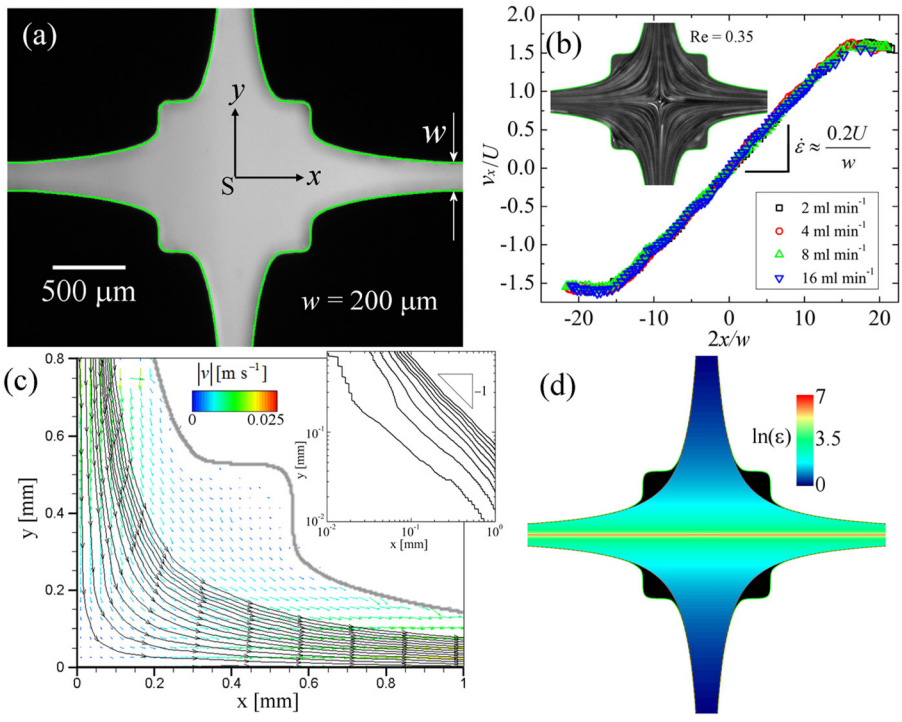

FIG. 9. The optimized cross-slots: (a) Light micrograph of an OSCER geometry with characteristic channel width $w = 200\,\mu$m and depth $d = 2$ mm ($\alpha = 10$). The numerically determined shape is superimposed in green. (b) Flow characterization with Newtonian fluid over a range of imposed flow rates shows a constant velocity gradient over the optimized region in good agreement with the numerical prediction. Inset shows streak imaging of fluorescent seed particles in a Newtonian fluid at low Re, providing a qualitative impression of the flow field. (c) Streamlines in one quadrant of the OSCER device superimposed on velocity vectors determined using μ-PIV. The Newtonian fluid consists of 66 wt. % glycerol in water; the colors of the velocity vectors indicate the velocity magnitude according to the scale bar. The inset shows the streamlines plotted on a log-log scale and indicates that the flow is close to ideally hyperbolic (slope −1). (d) Steady-state strain field in the OSCER device, calculated over the domain demarcated by the red dashed hyperbolae, and assuming the flow field is described by ideal planar elongation.

9(b). In addition, streamlines determined from flow velocimetry experiments have been shown to have close to the ideal hyperbolic form through a large portion of the device, i.e., away from the salient corners (which serve to self-lubricate the central flow), see Fig. 9(c). A calculation of the fluid strain, ε, based on the assumption of hyperbolicity gives the result shown in Fig. 9(d). Strain is constant along x and varies hyperbolically along y, diverging for $y = 0$. The strain exceeds $\varepsilon > 100$ within a 30 μm wide band ($|y| \leq 15\,\mu$m, or $|y| \leq w/13.3$) and exceeds $\varepsilon > 500$ within a 6 μm wide band ($|y| \leq 3\,\mu$m, or $|y| \leq w/66.7$).

The so-called OSCER has been tested using model non-shear thinning polymer solutions consisting of dilute, high molecular weight poly(ethylene oxide) (PEO) dissolved in an aqueous solvent.[24] Over a range of strain rates, highly localized and uniform birefringent strands have been observed to develop along the outflow axis, providing a clear visual demonstration of both the homogeneity of the flow field and the high strains available along the flow axis, see Fig. 10(a). Bulk pressure drop and local flow-induced birefringence measurements were used to assess the extensional viscosity, resulting in good agreement with each other, see Fig. 10(b). The experimental measurements also agreed well with model predictions using a finitely extensible non-linear elastic dumbbell (FENE) model, with parameters determined from the fluid rheology and the known characteristics of the polymer-solvent system.

The OSCER has also been used for the study of HA solutions.[189] It has been suggested that strain hardening of the synovial fluid may play a role in protecting joints such as the knee from high-load compressional impacts (such as running and jumping motions).[14] The compressional flow along the inlets of the OSCER device can be considered as a model of the squeeze flow between the joint surfaces of the knee during compressive motions and the experiments clearly show that HA solutions can undergo significant extension thickening under such conditions at physiologically relevant strain rates.[189]

Despite its advantages, the fabrication of the OSCER device with a quasi-2D aspect ratio required a rather specialized fabrication method (wire electrical discharge machining, wire-EDM).[24] Using this method, the smallest characteristic channel dimension was limited by the radius of the machining wire to $w \approx 200\,\mu$m. In the final geometry with the long optimized region ($15w$) shown in Fig. 9(a), it was difficult to achieve very high extensional rates with aqueous fluids in inertialess conditions. In fact, the experiments of Haward *et al.* were arrested for $\dot{\varepsilon} < 500\ s^{-1}$ due to the onset of flow instabilities.[24,189]

With the motivation of achieving higher extensional rates while minimizing inertia, and also of making the optimized cross-slot geometry accessible to the wider microfluidics community, Galindo-Rosales *et al.*[190] have recently investigated the fabrication of moderate aspect ratio ($0.5 \leq \alpha \leq 2$) devices in poly(dimethyl siloxane) (PDMS) using standard soft-lithography methods. Some examples of these 3D OSCER devices, with various aspect ratios and optimization

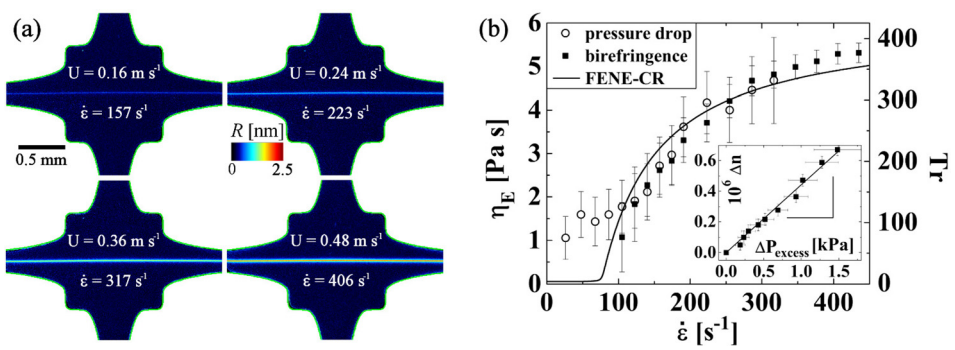

FIG. 10. (a) Birefringence observed with a dilute PEO solution in the OSCER device at the strain rates indicated in the images. Reprinted with permission from Haward *et al.*, Phys. Rev. Lett. **109**, 128301 (2012). Copyright 2012 The American Physical Society. (b) Extensional viscosity and Trouton ratio of the dilute PEO solution assessed using birefringence and pressure drop measurements and compared with the prediction of the FENE model. Inset shows a linear relationship between the birefringence and the excess pressure drop. Reprinted with permission from Haward *et al.*, Phys. Rev. Lett. **109**, 128301 (2012). Copyright 2012 The American Physical Society.

lengths, L_{ext}, are shown in Fig. 11. In general, the devices performed as expected with a quasi-homogeneous extension rate measured over L_{ext}. However, due to the low aspect ratios, the flow is rather inhomogeneous through the depth.[190] Devices fabricated in this way may have useful applications in microfluidic hydrodynamic trapping and stretching experiments[190] but are perhaps not ideal for the purposes of extensional rheometry.

C. Flow instabilities in stagnation point micro-devices

As previously mentioned, extensional rheometry experiments using the OSCER device were limited by the onset of flow instabilities encountered as the flow rate was increased.[24,189] Flow instabilities are a limiting factor in all kinds of rheometry, and it is important to characterize them in order to evaluate the operating space of a particular rheometer. The planar flow in the cross-slot device allows relatively straightforward flow visualization and therefore offers the opportunity to examine flow instabilities of viscoelastic fluids near a stagnation point.

Arratia *et al.*[191] originally reported a purely elastic flow instability in a microfluidic cross-slot with a dilute polymer solution consisting of high molecular weight poly(acrylamide) in an aqueous solvent. At low Wi and Re, the flow was steady and symmetric, but for flow at high $\mathrm{Wi} = 4.5$ (though still low $\mathrm{Re} < 10^{-2}$) a flow asymmetry developed in which the flow through each inlet divided unequally between the two outlets, see Fig. 12(a). At higher $\mathrm{Wi} \gtrsim 12.5$, the instability became time-dependent with broadband temporal fluctuations. The initial instability was characterized as a forward bifurcation, and this was confirmed by subsequent numerical simulations using the upper-convected Maxwell model performed at $\mathrm{Re} = 0$, see Fig. 12(b).[192] Using a FENE model, Rocha *et al.*[193] investigated the effects of the polymer concentration (as reflected by the ratio of polymer to solvent viscosity) and polymer chain extensibility on the onset of the bifurcation and found that the critical Weissenberg number was reduced as either the concentration or extensibility was increased. Recent experimental studies of these phenomena suggest that the onset conditions for steady asymmetric flows and time-dependent flows may strongly depend on the cross-slot aspect ratio; at low aspect ratios, the bounding walls have a stabilizing effect, preventing the transition to steady asymmetric flow and delaying the transition to time-dependence to higher Wi.[194] Similar instabilities have also been reported in shear thinning and shear banding wormlike micellar solutions, see Fig. 12(c), although different as yet unexplained scalings for the instability growth with Wi have been reported depending on the fluid formulation.[128,135,187,195] Recently, it has been suggested that this bifurcation phenomenon could serve as a numerical benchmark flow problem for viscoelastic fluids.[196] There is current debate over whether or not these purely elastic instabilities in extension-dominated flows are driven by the same mechanism of tension along curved streamlines that governs instabilities observed in viscometric rotational flows such as the Taylor-Couette geometry.[197–201]

Flow instabilities have also been investigated in the 2D OSCER device using a wide range of viscoelastic fluids composed of PEO and HA solutions of various molecular weight, concentration, and solvent viscosity in order to generate a range of several elasticity numbers $\mathrm{El} = \mathrm{Wi}/\mathrm{Re}$, see Fig. 13.[202] Fluids of high $\mathrm{El} > 1$ displayed purely elastic flow asymmetries for $\mathrm{Wi} \gtrsim 3$ similar to those reported previously by Arratia *et al.*[191] and Poole *et al.*,[192] see Fig. 13(a). However, as the elasticity number was reduced to $\mathrm{El} < 1$, instability occurred beyond a critical Re and was

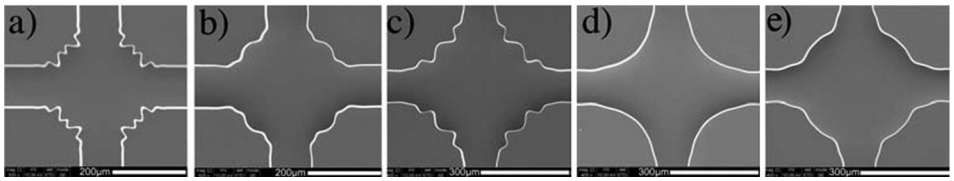

FIG. 11. Scanning electron micrographs of 3D OSCER geometries fabricated by soft lithography in PDMS with various aspect ratios and optimized over various length scales, L_{ext}: (a) $w = d = 100\,\mu\mathrm{m}$, $L_{ext} = 2w$, (b) $w = d = 100\,\mu\mathrm{m}$, $L_{ext} = 3w$, (c) $w = d = 100\,\mu\mathrm{m}$, $L_{ext} = 5w$, (d) $w = 2d = 100\,\mu\mathrm{m}$, $L_{ext} = 5w$, and (e) $w = 0.5d = 100\,\mu\mathrm{m}$, $L_{ext} = 5w$. Adapted with permission from Galindo-Rosales *et al.*, RSC Adv. **4**, 7799 (2014). Copyright 2014 The Royal Society of Chemistry.

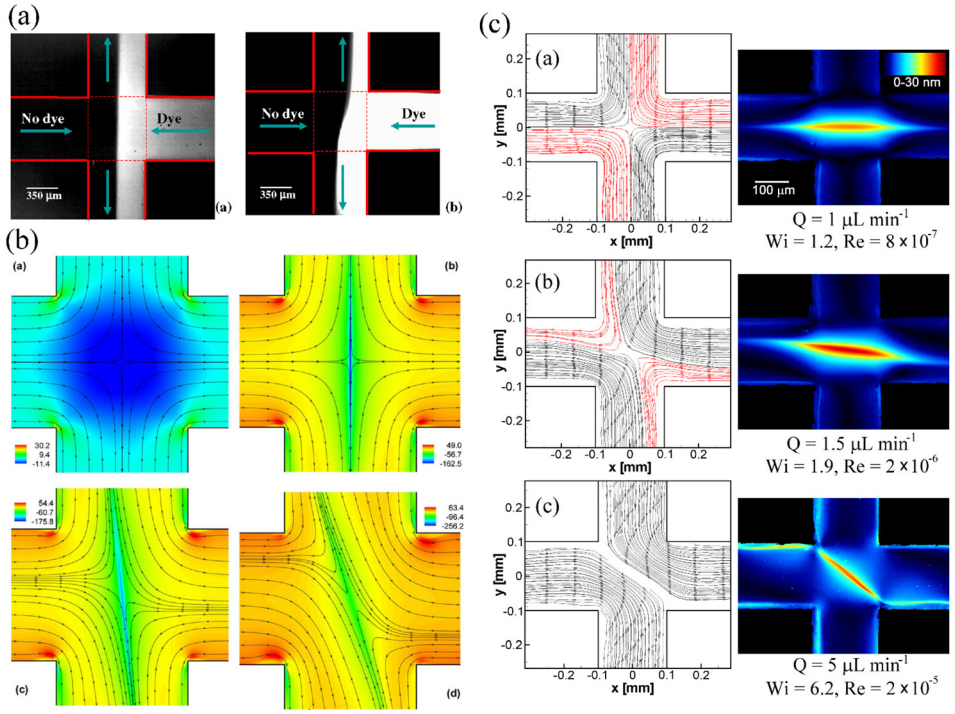

FIG. 12. Purely elastic flow instabilities in microfluidic cross-slot devices: (a) Fluorescence imaging of fluid flow in a cross-slot at $\mathrm{Re} < 10^{-2}$ performed with a Newtonian fluid (left) and a dilute poly(acrylamide) solution at $\mathrm{Wi} = 4.5$ (right). Reprinted with permission from Arratia *et al.*, Phys. Rev. Lett. **96**, 144502 (2006). Copyright 2006 The American Physical Society. (b) Numerical simulations of cross-slot flow at $\mathrm{Re} = 0$ of a Newtonian fluid and an upper-convected Maxwell fluid at $\mathrm{Wi} = 0.3$, 0.32, and 0.4 ((a)–(d), respectively). Outflow is along the vertical direction. Reprinted with permission from Poole *et al.*, Phys. Rev. Lett. **99**, 164503 (2007). Copyright 2007 The American Physical Society. (c) Flow streamlines (left) and corresponding flow birefringence images (right) for a wormlike micellar solution consisting of cetylpyridinium chloride and sodium salicylate (CPyCl-NaSal) at the Reynolds and Weissenberg numbers indicated. Outflow is along the horizontal direction. Reprinted with permission from S. J. Haward and G. H. McKinley, Phys. Rev. E **85**, 031502 (2012). Copyright 2012 The American Physical Society.

manifested as an oscillatory motion of the birefringent strand resulting in a varicose or sinuous appearing structure, see Fig. 13(b). Due to the clear importance of both inertia ($\mathrm{Re} > 10$) and elasticity ($\mathrm{El} > 1$), for the onset of this second class of instabilities, they were termed "inertio-elastic." A stability diagram for purely elastic and inertio-elastic instabilities in Wi-Re space was constructed (see Fig. 13(c)) where the region labelled "stable symmetric flow" indicates the operating space of the OSCER device for performing rheometric measurements.[202]

It is worthwhile to mention that purely inertial flow instabilities in cross-slot devices have also been investigated, chiefly in the context of microfluidic mixing of Newtonian fluids at low to moderate Re.[139–141] In this case, a steady symmetry breaking bifurcation has been observed for flow above a critical Reynolds number ($20 \lesssim \mathrm{Re}_c \lesssim 100$), resulting in the formation of a 3D spiral vortex structure aligned along the outlet channel. Within the spiral, the mixing between the two incoming fluid streams is significantly enhanced.[140,141] Recently, experiments and numerical simulations have shown that value of Re_c for the transition depends strongly on the aspect ratio of the cross-slots and occurs near a tricritical point, switching from a forward (supercritical) to a backward (subcritical) bifurcation as the aspect ratio is increased above $\alpha \approx 0.5$.[141] Much more work is required to understand the physical mechanism underlying these transitions, their dynamics, and also how they are affected by fluid elasticity.[138,203,204]

V. SUMMARY AND PERSPECTIVES

In this review, we have presented an overview of current methods of applying extensional deformations to mobile fluids, focussing on the use of stagnation point flows in microfluidic

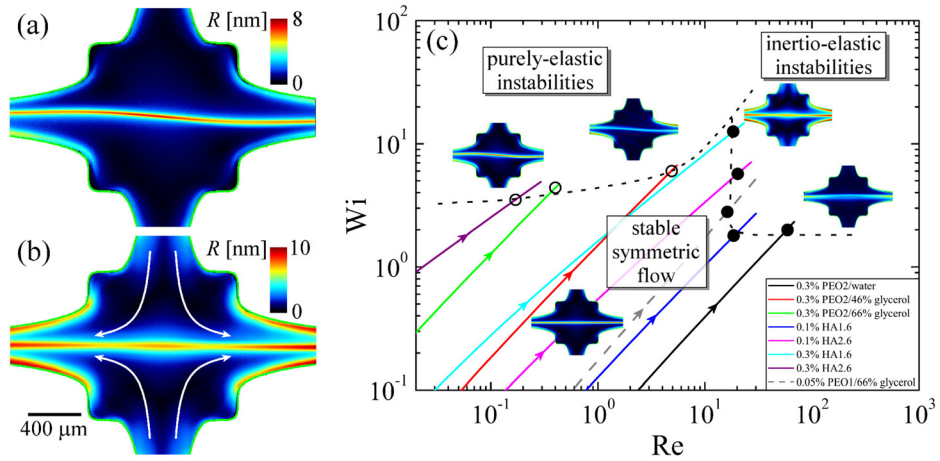

FIG. 13. Purely elastic and inertio-elastic flow instabilities in the OSCER device. (a) A steady purely elastic flow instability in 0.3 wt. % solution of a 2.6 MDa hyaluronic acid flowing at Re = 0.3, Wi = 5, and El = 16.7. Reprinted with permission from Phys. Fluids **25**, 083104 (2013). Copyright 2013 AIP Publishing LLC. (b) A sinuous inertio-elastic instability in a 0.3 wt. % solution of a 1.6 MDa hyaluronic acid flowing at Re = 30.6, Wi = 18, and El = 0.6. Reprinted with permission from Phys. Fluids **25**, 083104 (2013). Copyright 2013 AIP Publishing LLC. (c) Stability map for viscoelastic fluids in Wi-Re space in the OSCER device. The colored lines indicate the trajectories of different test fluids through the dimensionless parameter space as the flow rate is varied. Reprinted with permission from Phys. Fluids **25**, 083104 (2013). Copyright 2013 AIP Publishing LLC.

devices (i.e., the cross-slots), which can probe the extensional rheological response of particularly low viscosity and low elasticity fluids using small sample volumes. Recent advances in cross-slot extensional rheometry such as the use of micro-oscillatory flow (EFOR) and the numerical optimization of the geometric shape of the cross-slots (OSCER) have been discussed. The combination of experiments and numerical simulations in the development of the OSCER has resulted in a major stride towards the goal of achieving a true planar extensional rheometer. An obvious next step in the development of microfluidic stagnation point rheometry is to combine the OSCER geometry with the oscillatory micropumps of the EFOR. In principle, this is trivial to do, but hardware modifications are required in order to permit a useful range of extension rates. This will include enhancement of the operating range of the micropumps along with miniaturization of the OSCER geometry. From a practical perspective, miniaturization of the OSCER device is highly desirable to further reduce required sample volumes and minimize inertia. Recent advances in 3D printing are envisioned as a promising solution for achieving the fabrication of devices with microfluidic lengthscales and the high aspect ratios required of rheometric fluidic devices. As with any rheometric technique, the operating range of the cross-slot type extensional rheometer is limited by flow instabilities. These turn out to be interesting dynamical phenomena in their own right, which are affected by a wide range of fluid parameters (e.g., viscosity, elasticity, and degree of shear-thinning) and are only just being characterized in any detail. A combination of experiments, numerical simulations, and theory will be required to achieve a thorough understanding of the physical mechanisms at play.

ACKNOWLEDGMENTS

The support of Okinawa Institute of Science and Technology Graduate University, with funding from the Cabinet Office, Government of Japan, is gratefully acknowledged. Dr. Francesco del Giudice is acknowledged for a careful and critical reading of the manuscript.

[1]D. V. Boger, Annu. Rev. Fluid Mech. **19**, 157 (1987).
[2]A. L. Yarin, *Free Liquid Jets and Films: Hydrodynamics and Rheology* (Longman, Harlow, 1993).
[3]R. Cressely and R. Hocquart, Opt. Acta **27**, 699 (1980).
[4]A. Ziabicki, *Fundamentals of Fibre Formation* (Wiley, London, 1976).
[5]S. Middleman, *Fundamentals of Polymer Processing* (McGraw-Hill, New York, 1977).
[6]P. S. Virk and H. Baher, Chem. Eng. Sci. **25**, 1183 (1970).

[7]A. J. Müller and A. E. Sáez, in *Flexible Polymer Chains in Elongational Flow*, edited by T. Q. Nguyen and H.-H. Kausch (Springer, Berlin, 1999), pp. 335–393.
[8]S. L. Shenoy, W. D. Bates, H. L. Frisch, and G. E. Wnek, Polymer **46**, 3372 (2005).
[9]*Inkjet Technology for Digital Fabrication*, edited by I. A. Hutchings and G. D. Martin (Wiley, UK, 2013).
[10]P. C. Sousa, F. T. Pinho, M. S. N. Oliveira, and M. A. Alves, Biomicrofluidics **5**, 014108 (2011).
[11]M. Brust, C. Shaefer, R. Doerr, L. Pan, M. Garcia, P. E. Arratia, and C. Wagner, Phys. Rev. Lett. **110**, 078305 (2013).
[12]P. P. Bhat, S. Appathurai, M. T. Harris, M. Pasquali, G. H. McKinley, and O. A. Basaran, Nat. Phys. **6**, 625 (2010).
[13]S. J. Haward, J. A. Odell, M. Berry, and T. Hall, Rheol. Acta **50**, 869 (2011).
[14]C. Backus, S. P. Carrington, L. R. Fisher, J. A. Odell, and D. A. Rodrigues, in *Hyaluronan Volume 1: Chemical, Biochemical and Biological Aspects*, edited by J. F. Kennedy, G. O. Phillips, P. A. Williams, and V. C. Hascall (Woodhead Publishing Ltd., Cambridge, 2002), pp. 209–218.
[15]S. J. Haward, Biopolymers **101**, 287 (2014).
[16]P. G. De Gennes, J. Chem. Phys. **60**, 5030 (1974).
[17]A. Keller and J. A. Odell, Colloid Polym. Sci. **263**, 181 (1985).
[18]R. G. Larson and J. J. Magda, Macromolecules **22**, 3004 (1989).
[19]T. T. Perkins, D. E. Smith, and S. Chu, Science **276**, 2016 (1997).
[20]F. T. Trouton, Proc. R. Soc. London, Ser. A **77**, 426 (1906).
[21]G. K. Batchelor, J. Fluid Mech. **44**, 419 (1970).
[22]D. F. James and K. Walters, in *Techniques of Rheological Measurement*, edited by A. A. Collyer (Elsevier, New York, 1994), pp. 33–53.
[23]D. F. James and T. Sridhar, J. Rheol. **39**, 713 (1995).
[24]S. J. Haward, M. S. N. Oliveira, M. A. Alves, and G. H. McKinley, Phys. Rev. Lett. **109**, 128301 (2012).
[25]L. Gaume and Y. Forterre, PLoS One **2**, e1185 (2007).
[26]V. Sahni, T. A. Blackledge, and A. Dhinojwala, Nat. Commun. **1**, 1 (2010).
[27]P. Erni, M. Varagnat, C. Clasen, J. Crest, and G. H. McKinley, Soft Matter **7**, 10889 (2011).
[28]N. Kojic, J. Bico, C. Clasen, and G. H. McKinley, J. Exp. Biol. **209**, 4355 (2006).
[29]G. W. Scott Blair, S. J. Folley, F. H. Malpress, and F. M. V. Coppen, Biochem. J. **35**, 1039 (1941).
[30]J. R. Stokes and G. A. Davies, Biorheology **44**, 141 (2007).
[31]H. A. Barnes, J. F. Hutton, and K. Walters, *An Introduction to Rheology* (Elsevier, Amsterdam, 1993).
[32]C. W. Macosko, *Rheology: Principles, Measurements and Applications* (Wiley, New York, 1994).
[33]C. J. S. Petrie, J. Non-Newtonian Fluid Mech. **137**, 15 (2006).
[34]C. J. S. Petrie, J. Non-Newtonian Fluid Mech. **70**, 205 (1997).
[35]D. E. Smith and S. Chu, Science **281**, 1335 (1998).
[36]T. M. Squires and S. R. Quake, Rev. Mod. Phys. **77**, 977 (2005).
[37]H. A. Stone, A. D. Stroock, and A. Ajdari, Annu. Rev. Fluid Mech. **36**, 381 (2004).
[38]R. Langer and D. A. Tirrell, Nature **428**, 487 (2004).
[39]G. M. Whitesides, Nature **442**, 368 (2006).
[40]E. A. Sackmann, A. L. Fulton, and D. J. Beebe, Nature **507**, 181 (2014).
[41]A. Bazilevsky, V. Entov, and A. Rozhkov, in *Proceedings of the 3rd European Rheology Conference*, edited by D. R. Oliver (Elsevier, New York, 1990), pp. 41–43.
[42]V. Tirtaatmadja and T. Sridhar, J. Rheol. **37**, 1081 (1993).
[43]S. L. Anna, G. H. McKinley, D. C. Nguyen, T. Sridar, S. J. Muller, J. Huang, and D. F. James, J. Rheol. **45**, 83 (2001).
[44]G. H. McKinley and T. Sridhar, Annu. Rev. Fluid Mech. **34**, 375 (2002).
[45]T. R. Tuladhar and M. R. Mackley, J. Non-Newtonian Fluid Mech. **148**, 97 (2008).
[46]S. H. Spiegelberg and G. H. McKinley, J. Non-Newtonian Fluid Mech. **67**, 49 (1996).
[47]A. Bazilevsky, V. Entov, A. Rozhkov, and A. L. Yarin, in *Proceedings of the 3rd European Rheology Conference*, edited by D. R. Oliver (Elsevier, New York, 1990), pp. 44–46.
[48]O. Regev, E. Vandebril, E. Zussmann, and C. Clasen, Polymer **51**, 2611 (2010).
[49]V. M. Entov and E. J. Hinch, J. Non-Newtonian Fluid Mech. **72**, 31 (1997).
[50]S. L. Anna and G. H. McKinley, J. Rheol. **45**, 115 (2001).
[51]D. T. Papageorgiou, Phys. Fluids **7**, 1529 (1995).
[52]M. S. N. Oliveira and G. H. McKinley, Phys. Fluids **17**, 071704 (2005).
[53]M. S. N. Oliveira, R. Yeh, and G. H. McKinley, J. Non-Newtonian Fluid Mech. **137**, 137 (2006).
[54]L. E. Rodd, T. P. Scott, J. J. Cooper-White, and G. H. McKinley, Appl. Rheol. **15**, 12 (2005).
[55]L. Campo-Deaño and C. Clasen, J. Non-Newtonian Fluid Mech. **165**, 1688 (2010).
[56]W. C. Nelson, H. P. Kavehpour, and C. J. Kim, Lab Chip **11**, 2424 (2011).
[57]P. K. Bhattacharjee, A. G. McDonnell, R. Prabhakar, L. Y. Yeo, and J. R. Friend, New J. Phys. **13**, 023005 (2011).
[58]S. R. V. Rao, C. Kalelkar, and P. A. Pullarkat, Rev. Sci. Instrum. **84**, 105107 (2013).
[59]A. G. McDonnell, T. C. Gopesh, J. Lo, M. O'Bryan, L. Y. Yeo, J. R. Friend, and R. Prabhakar, Soft Matter **11**, 4658 (2015).
[60]F. J. Galindo-Rosales, M. A. Alves, and M. S. N. Oliveira, Microfluid. Nanofluid. **14**, 1 (2013).
[61]V. Sharma, S. J. Haward, J. Serdy, B. Keshavarz, A. Soderlund, P. Threlfall-Holmes, and G. H. McKinley, Soft Matter **11**, 3251 (2015).
[62]B. Keshavarz, V. Sharma, E. C. Houze, M. R. Koerner, J. R. Moore, P. M. Cotts, P. Threlfall-Holmes, and G. H. McKinley, J. Non-Newtonian Fluid Mech. **222**, 171 (2015).
[63]C. Clasen, Korea-Aust. Rheol. J. **22**, 331 (2010).
[64]F. N. Cogswell, Polym. Eng. Sci. **12**, 64 (1972).
[65]F. N. Cogswell, J. Non-Newtonian Fluid Mech. **4**, 23 (1978).
[66]D. F. James and J. H. Saringer, J. Non-Newtonian Fluid Mech. **11**, 317 (1982).
[67]R. Evans and K. Walters, J. Non-Newtonian Fluid Mech. **20**, 11 (1986).
[68]G. H. McKinley, W. P. Raiford, R. A. Brown, and R. C. Armstrong, J. Fluid Mech. **223**, 411 (1991).
[69]L. M. Quinzani, R. C. Armstrong, and R. A. Brown, J. Non-Newtonian Fluid Mech. **52**, 1 (1994).
[70]J. P. Rothstein and G. H. McKinley, J. Non-Newtonian Fluid Mech. **86**, 61 (1999).

[71]S. Nigen and K. W. Walters, J. Non-Newtonian Fluid Mech. **102**, 343 (2002).
[72]M. S. N. Oliveira, M. A. Alves, F. T. Pinho, and G. H. McKinley, Exp. Fluids **43**, 437 (2007).
[73]D. M. Binding and K. Walters, J. Non-Newtonian Fluid Mech. **30**, 233 (1988).
[74]J. P. Rothstein and G. H. McKinley, J. Non-Newtonian Fluid Mech. **98**, 33 (2001).
[75]D. Hunkeler, T. Q. Nguyen, and H. H. Kausch, Polymer **37**, 4257 (1996).
[76]G. Yu, T. Q. Nguyen, and H. H. Kausch, J. Polym. Sci., Part B: Polym. Phys. **36**, 1483 (1998).
[77]A. M. Afonso, P. J. Oliveira, F. T. Pinho, and M. A. Alves, J. Fluid Mech. **677**, 272 (2011).
[78]M. Nystrom, H. R. Tamaddon-Jahromi, M. Stading, and M. F. Webster, Rheol. Acta **51**, 713 (2012).
[79]R. I. Tanner and K. Walters, *Rheology: An Historical Perspective* (Elsevier, Amsterdam, 1998).
[80]O. Hassager, J. Non-Newtonian Fluid Mech. **29**, 337 (1988).
[81]L. M. Quinzani, R. C. Armstrong, and R. A. Brown, J. Rheol. **39**, 1201 (1995).
[82]R. G. Owens and N. T. Phillips, *Computational Rheology* (Imperial College Press, London, 2002).
[83]L. E. Rodd, T. P. Scott, D. V. Boger, J. J. Cooper-White, and G. H. McKinley, J. Non-Newtonian Fluid Mech. **129**, 1 (2005).
[84]L. E. Rodd, J. J. Cooper-White, D. V. Boger, and G. H. McKinley, J. Non-Newtonian Fluid Mech. **143**, 170 (2007).
[85]M. S. N. Oliveira, P. J. Oliveira, F. T. Pinho, and M. A. Alves, J. Non-Newtonian Fluid Mech. **147**, 92 (2007).
[86]Z. Li, X.-F. Yuan, S. J. Haward, J. A. Odell, and S. Yeates, J. Non-Newtonian Fluid Mech. **166**, 951 (2011).
[87]Z. Li and S. J. Haward, Microfluid. Nanofluid. **19**, 1123 (2015).
[88]S. J. Haward, Z. Li, D. Lighter, B. Thomas, J. A. Odell, and X.-F. Yuan, J. Non-Newtonian Fluid Mech. **165**, 1654 (2010).
[89]S. Gulati, D. Liepmann, and S. J. Muller, Phys. Rev. E **78**, 036314 (2008).
[90]O. L. Hemminger, P. E. Boukany, S.-Q. Wang, and L. J. Lee, J. Non-Newtonian Fluid Mech. **165**, 1613 (2010).
[91]L. E. Rodd, D. Lee, K. H. Ahn, and J. J. Cooper-White, J. Non-Newtonian Fluid Mech. **165**, 1189 (2010).
[92]Z. Li, X.-F. Yuan, S. J. Haward, J. A. Odell, and S. Yeates, Rheol. Acta **50**, 277 (2011).
[93]A. S. Lubansky and M. T. Matthews, J. Rheol. **59**, 835 (2015).
[94]L. Campo-Deaño, F. J. Galindo-Rosales, F. T. Pinho, M. A. Alves, and M. S. N. Oliveira, J. Non-Newtonian Fluid Mech. **166**, 1286 (2011).
[95]T. J. Ober, S. J. Haward, C. J. Pipe, J. Soulages, and G. H. McKinley, Rheol. Acta **52**, 529 (2013).
[96]J. Wang and D. F. James, J. Rheol. **55**, 1103 (2011).
[97]P. E. Arratia, J. P. Gollub, and D. J. Durian, Phys. Rev. E **77**, 036309 (2008).
[98]P. E. Arratia, L.-A. Cramer, J. P. Gollub, and D. J. Durian, New J. Phys. **11**, 115006 (2009).
[99]G. Juarez and P. E. Arratia, Soft Matter **7**, 9444 (2011).
[100]R. G. Larson, AIP Conf. Proc. **982**, 419 (2008).
[101]G. I. Taylor, Proc. R. Soc. London, Ser. A **146**, 501 (1934).
[102]D. G. Crowley, F. C. Frank, and M. R. Mackley, J. Polym. Sci., Part B: Polym. Phys. **14**, 1111 (1976).
[103]G. G. Fuller and L. G. Leal, Rheol. Acta **19**, 580 (1980).
[104]P. N. Dunlap and L. G. Leal, J. Non-Newtonian Fluid Mech. **23**, 5 (1987).
[105]R. R. Lagnado and L. G. Leal, Exp. Fluids **9**, 25 (1990).
[106]S. D. Hudson, F. R. Phelan, M. D. Handler, J. T. Cabral, K. B. Migler, and E. J. Amis, Appl. Phys. Lett. **85**, 335 (2004).
[107]J. S. Lee, R. Dylla-Spears, N. P. Teclemariam, and S. J. Muller, Appl. Phys. Lett. **90**, 074103 (2007).
[108]J. Deschamps, V. Kantsler, E. Segre, and V. Steinberg, Proc. Natl. Acad. Sci. U.S.A. **106**, 11444 (2009).
[109]J. S. Lee, E. S. G. Shaqfeh, and S. J. Muller, Phys. Rev. E **75**, 040802 (2007).
[110]Y.-N. Young, J. Blawzdiewicz, V. Cristini, and R. H. Goodman, J. Fluid Mech. **607**, 209 (2008).
[111]J. T. Wang, J. J. Han, and D. M. Yu, Eng. Anal. Boundary Elem. **36**, 1453 (2012).
[112]J. Guan, J. Liu, X. Li, J. Tao, and J. Wang, Z. Angew. Math. Phys. **66**, 149 (2015).
[113]F. C. Frank, A. Keller, and M. R. Mackley, Polymer **12**, 467 (1971).
[114]A. J. Müller, J. A. Odell, and A. Keller, J. Non-Newtonian Fluid Mech. **30**, 99 (1988).
[115]J. A. Odell, A. J. Müller, K. A. Nahr, and A. Keller, Macromolecules **23**, 3092 (1990).
[116]G. G. Fuller, C. A. Cathey, B. Hubbard, and B. E. Zebrowski, J. Rheol. **31**, 235 (1987).
[117]C. A. Cathey and G. G. Fuller, J. Non-Newtonian Fluid Mech. **30**, 303 (1988).
[118]R. K. Prud'homme and G. G. Warr, Langmuir **10**, 3419 (1994).
[119]C. G. Hermansky and D. V. Boger, J. Non-Newtonian Fluid Mech. **56**, 1 (1995).
[120]S. L. Ng, R. P. Mun, D. V. Boger, and D. F. James, J. Non-Newtonian Fluid Mech. **65**, 291 (1996).
[121]C.-M. Chen and G. G. Warr, Langmuir **13**, 1374 (1997).
[122]P. Dontula, M. Pasquali, L. E. Scriven, and C. W. Macosko, Rheol. Acta **36**, 429 (1997).
[123]O. Scrivener, C. Berner, R. Cressely, R. Hocquart, R. Sellin, and N. S. Vlachos, J. Non-Newtonian Fluid Mech. **5**, 475 (1979).
[124]G. G. Fuller, *Optical Rheometry of Complex Fluids* (Oxford University Press, New York, 1995).
[125]K. D. Coventry and M. R. Mackley, J. Rheol. **52**, 401 (2008).
[126]S. J. Haward, V. Sharma, and J. A. Odell, Soft Matter **7**, 9908 (2011).
[127]D. Auhl, D. M. Hoyle, D. Hassell, T. D. Lord, O. G. Harlen, M. R. Mackley, and T. C. B. McLeish, J. Rheol. **55**, 875 (2011).
[128]S. J. Haward and G. H. McKinley, Phys. Rev. E **85**, 031502 (2012).
[129]J. Soulages, T. Schweizer, D. C. Venerus, M. Kröger, and H. C. Öttinger, J. Non-Newtonian Fluid Mech. **154**, 52 (2008).
[130]A. Abedijaberi, J. Soulages, M. Kröger, and B. Khomami, Rheol. Acta **48**, 97 (2009).
[131]M. J. Miles and A. Keller, Polymer **21**, 1295 (1980).
[132]K. Gardner, E. R. Pike, M. J. Miles, A. Keller, and K. Tanaka, Polymer **23**, 1435 (1982).
[133]J. A. Odell and A. Keller, J. Polym. Sci., Part B: Polym. Phys. **24**, 1889 (1986).
[134]R. Dylla-Spears, J. E. Townsend, L. Jen-Jacobson, L. L. Sohn, and S. J. Muller, Lab Chip **10**, 1543 (2010).
[135]J. A. Pathak and S. D. Hudson, Macromolecules **39**, 8782 (2006).
[136]W. R. Dean, Philos. Mag. **5**, 673 (1928).

[137]V. N. Kalashnikov and M. G. Tsiklauri, Fluid Dyn. **26**, 161 (1991).
[138]V. N. Kalashnikov and M. G. Tsiklauri, J. Non-Newtonian Fluid Mech. **48**, 215 (1993).
[139]N. Ait Mouheb, A. Montillet, C. Solliec, J. Havlica, P. Legentilhomme, J. Comiti, and J. Tihon, Microfluid. Nanofluid. **10**, 1185 (2011).
[140]N. Ait Mouheb, D. Malsch, A. Montillet, C. Solliec, and T. Henkel, Chem. Eng. Sci. **68**, 278 (2012).
[141]S. J. Haward, R. J. Poole, M. A. Alves, P. J. Oliveira, N. Goldenfeld, and A. Q. Shen, Phys. Rev. E **93**, 031101 (2016).
[142]B. H. Zimm, J. Chem. Phys. **24**, 269 (1956).
[143]C. M. Schroeder, H. P. Babcock, E. S. G. Shaqfeh, and S. Chu, Science **301**, 1515 (2003).
[144]E. S. G. Shaqfeh, J. Non-Newtonian Fluid Mech. **130**, 1 (2005).
[145]P. A. Stone, S. D. Hudson, P. Dalhaimer, D. E. Discher, E. J. Amis, and K. B. Migler, Macromolecules **39**, 7144 (2006).
[146]W. Xu and S. J. Muller, Lab Chip **11**, 435 (2011).
[147]M. Tanyeri, E. M. Johnson-Chavarria, and C. M. Schroeder, Appl. Phys. Lett. **96**, 224101 (2010).
[148]M. Tanyeri, M. Ranka, N. Sittipolkul, and C. M. Schroeder, Lab Chip **11**, 1786 (2011).
[149]M. Tanyeri and C. M. Schroeder, Nano Lett. **13**, 2357 (2013).
[150]E. M. Johnson-Chavarria, U. Agrawal, M. Tanyeri, T. E. Kuhlman, and C. M. Schroeder, Lab Chip **14**, 2688 (2014).
[151]A. Shenoy, M. Tanyeri, and C. M. Schroeder, Microfluid. Nanofluid. **18**, 1055 (2015).
[152]T. G. G. Toh, C. Yang, Z. Wang, and N.-T. Nguyen, Lab Chip **16**, 368 (2016).
[153]N. Nève, S. S. Kohles, S. R. Winn, and D. C. Tretheway, Cell. Mol. Bioeng. **3**, 213 (2010).
[154]D. R. Gossett, H. T. K. Tse, S. A. Lee, Y. Ying, A. G. Lindgren, O. O. Yang, J. Rao, A. T. Clark, and D. Di Carlo, Proc. Natl. Acad. Sci. U.S.A. **109**, 7630 (2012).
[155]S. Cha, T. Shin, S. S. Lee, W. Shim, G. Lee, S. J. Lee, Y. Kim, and J. M. Kim, Anal. Chem. **84**, 10471 (2012).
[156]H. T. K. Tse, D. R. Gossett, Y. S. Moon, M. Masaeli, M. Sohsman, Y. Ying, K. Mislick, R. P. Adams, J. Rao, and D. Di Carlo, Sci. Transl. Med. **5**, 212ra163 (2013).
[157]Y. Henon, G. J. Sheard, and A. Fouras, RSC Adv. **4**, 36079 (2014).
[158]E. J. Lim, T. J. Ober, J. E. Edd, S. P. Desai, D. Neal, K. W. Bong, P. S. Doyle, G. H. McKinley, and M. Toner, Nat. Commun. **5**, 4120 (2014).
[159]C. de Loubens, J. Deschamps, G. Boedec, and M. Leonetti, J. Fluid Mech. **767**, R3 (2015).
[160]V. Kantsler, E. Segre, and V. Steinberg, Phys. Rev. Lett. **99**, 178102 (2007).
[161]V. Kantsler, E. Segre, and V. Steinberg, Phys. Rev. Lett. **101**, 048101 (2008).
[162]J. A. Odell, in *Handbook of Experimental Fluid Mechanics*, edited by C. Tropea, A. L. Yarin, and J. F. Foss (Springer-Verlag, Heidelberg, 2007), pp. 724–732.
[163]M. Kisilak, H. Anderson, N. S. Babcock, M. R. Stetzer, S. H. J. Idziak, and E. B. Sirota, Rev. Sci. Instrum. **72**, 4305 (2001).
[164]J. Penfold, E. Staples, I. Tucker, P. Carroll, J. S. Cowan, G. Lawton, S. Amin, A. Ferrante, and N. Ruddock, J. Phys. Chem. B **110**, 1073 (2006).
[165]V. Sharma, A. Jaishankar, Y.-C. Wang, and G. H. McKinley, Soft Matter **7**, 5150 (2011).
[166]A. Jaishankar, V. Sharma, and G. H. McKinley, Soft Matter **7**, 7623 (2011).
[167]P. J. Flory, *Principles of Polymer Chemistry* (Cornell University Press, Ithaca, New York, 1953).
[168]R. G. Schipper, E. Silletti, and M. H. Vingerhoeds, Arch. Oral Biol. **52**, 1114 (2007).
[169]J. A. Odell, A. Keller, and Y. Rabin, J. Chem. Phys. **88**, 4022 (1988).
[170]J. A. Odell and S. P. Carrington, J. Non-Newtonian Fluid Mech. **137**, 110 (2006).
[171]S. J. Haward, PLoS One **9**, e92867 (2014).
[172]S. J. Haward, J. A. Odell, Z. Li, and X.-F. Yuan, Rheol. Acta **49**, 633 (2010).
[173]S. J. Haward, J. A. Odell, Z. Li, and X.-F. Yuan, Rheol. Acta **49**, 781 (2010).
[174]P. S. Doyle, E. S. G. Shaqfeh, G. H. McKinley, and S. H. Spiegelberg, J. Non-Newtonian Fluid Mech. **76**, 79 (1998).
[175]D. C. Venerus, S. H. Zhu, and H.-C. Öttinger, J. Rheol. **43**, 795 (1999).
[176]J. M. Li, W. R. Burghardt, B. Yang, and B. Khomami, J. Non-Newtonian Fluid Mech. **91**, 189 (2000).
[177]C. C. Hsieh and R. G. Larson, J. Rheol. **48**, 995 (2004).
[178]L. B. Dahl, I. M. Dahl, A. Engstrom-Laurent, and K. Granath, Ann. Rheum. Dis. **44**, 817 (1985).
[179]B. M. Praest, H. Greiling, and R. Kock, Clin. Chim. Acta **266**, 117 (1997).
[180]B. K. Rubin, Pediatr. Respir. Rev. **8**, 4 (2007).
[181]A. L. Innes, S. D. Carrington, D. J. Thornton, S. Kirkham, K. Rousseau, R. H. Dougherty, W. W. Raymond, G. H. Caughey, S. H. Muller, and J. V. Fahy, Am. J. Respir. Crit. Care Med. **180**, 203 (2009).
[182]S. Rossi, M. Marciello, M. C. Bonferoni, F. Ferrari, G. Sandri, C. Dacarro, P. Grisoli, and C. Caramella, Eur. J. Pharm. Biopharm. **74**, 248 (2010).
[183]S. J. Haward, Rheol. Acta **49**, 1219 (2010).
[184]R. C. H. van der Burgt, P. D. Anderson, J. M. J. den Toonder, and F. N. van de Vosse, Sens. Actuators, A **220**, 221 (2014).
[185]F. R. Phelan, N. R. Hughes, and J. A. Pathak, Phys. Fluids **20**, 023101 (2008).
[186]F. R. Phelan, P. Kutty, and J. A. Pathak, Microfluid. Nanofluid. **5**, 101 (2008).
[187]S. J. Haward, T. J. Ober, M. S. N. Oliveira, M. A. Alves, and G. H. McKinley, Soft Matter **8**, 536 (2012).
[188]M. A. Alves, AIP Conf. Proc. **1027**, 240 (2008).
[189]S. J. Haward, A. Jaishankar, M. S. N. Oliveira, M. A. Alves, and G. H. McKinley, Biomicrofluidics **7**, 044108 (2013).
[190]F. J. Galindo-Rosales, M. S. N. Oliveira, and M. A. Alves, RSC Adv. **4**, 7799 (2014).
[191]P. E. Arratia, C. C. Thomas, J. Diorio, and J. P. Gollub, Phys. Rev. Lett. **96**, 144502 (2006).
[192]R. J. Poole, M. A. Alves, and P. J. Oliveira, Phys. Rev. Lett. **99**, 164503 (2007).
[193]G. N. Rocha, R. J. Poole, M. A. Alves, and P. J. Oliveira, J. Non-Newtonian Fluid Mech. **156**, 58 (2009).
[194]P. C. Sousa, F. T. Pinho, M. S. N. Oliveira, and M. A. Alves, Soft Matter **11**, 8856 (2015).
[195]N. Dubash, P. Cheung, and A. Q. Shen, Soft Matter **8**, 5847 (2012).
[196]F. A. Cruz, R. J. Poole, A. M. Afonso, F. T. Pinho, P. J. Oliveira, and M. A. Alves, J. Non-Newtonian Fluid Mech. **214**, 57 (2014).

[197]S. J. Muller, R. G. Larson, and E. S. G. Shaqfeh, Rheol. Acta **28**, 499 (1989).
[198]P. Pakdel and G. H. McKinley, Phys. Rev. Lett. **77**, 2459 (1996).
[199]G. H. McKinley, P. Pakdel, and A. Öztekin, J. Non-Newtonian Fluid Mech. **67**, 19 (1996).
[200]S. J. Muller, Korea-Aust. Rheol. J **20**, 117 (2008).
[201]F. J. Galindo-Rosales, L. Campo-Deaño, P. C. Sousa, V. M. Ribeiro, M. S. N. Oliveira, M. A. Alves, and F. T. Pinho, Exp. Therm. Fluid Sci. **59**, 128 (2014).
[202]S. J. Haward and G. H. McKinley, Phys. Fluids **25**, 083104 (2013).
[203]M. T. Islam, S. A. Vanapalli, and M. J. Solomon, Macromolecules **37**, 1023 (2004).
[204]S. A. Vanapalli, S. L. Ceccio, and M. J. Solomon, Proc. Natl. Acad. Sci. U.S.A. **103**, 16660 (2006).